Manuscript Click here to view linked References

Experiment and Multiphysics Simulation of Inductively Heated Concrete Thermal Energy Storage Systems

Liuhui Tu, Guillermo A. Narsilio, Tuan Nguyen[1]

Department of Infrastructure Engineering, The University of Melbourne, VIC 3010, Australia

Abstract

This study presents an experimental and multiphysics modelling investigation of inductively heated concrete thermal energy storage (CTES) systems incorporating different heat transfer fluid (HTF) passages. Three HTF designs, including single-tube (ST), multiple-tube (MT), and triply periodic minimal surface (TPMS)-based heat exchanger structures, were experimentally evaluated under different induction heating conditions. Thermal charging to 260 °C was achieved using a 55 V, 50 kHz high-frequency induction heating system that takes advantage of the metallic structures embedded in the CTES, while discharging was realised via forced-convection airflow. Temperature evolution and pressure drop were measured to evaluate the thermal–hydraulic behaviour of the CTES modules. Furthermore, a coupled multiphysics numerical model integrating electromagnetic induction, heat transfer, and fluid flow was developed and validated against these experimental results. A ±5% coil-current sensitivity analysis across ST, MT, and TPMS identified 110 A and 130 A as the most representative currents for the 200 mm and 150 mm coils tested. Advanced metallic heat exchanger geometries significantly improved inductive charging over the conventional ST configuration. For the 200 mm coil, MT and TPMS advanced configurations increased maximum charging power by about 94% and 82%. The 150 mm coil further boosted charging, with TPMS showing the best performance. The parametric modelling shows that improved induction coupling and larger heat-transfer surfaces with helical fins helped achieve comparable charging/discharging power and energy storage. The induction-assisted CTES system shows strong potential for flexible thermal energy storage and offers new insights into integrating HTF metallic structures with induction heating.

Keywords: Inductive heating; Concrete Thermal Energy Storage; Multiphysics modelling; Triply periodic minimal surface; Heat transfer enhancement; Metallic fins

[1] Corresponding author. E-mail address: tuan.nguyen@unimelb.edu.au (Tuan Nguyen).

Nomenclature

Symbol	Definition	Unit
	Electromagnetic field	
$\mathbf{B}$	Magnetic flux density	T
$\mathbf{D}$	Electric displacement field	Cm^{-2}
$\mathbf{E}$	Electric field intensity	Vm^{-1}
f	Excitation current frequency	Hz
$\mathbf{H}$	Magnetic field intensity	Am^{-1}
$\mathbf{J}$	Electric current density	Am^{-2}
q_J	Volumetric Joule heat generation	Wm^{-3}
δ	Skin depth	m
ε_0	Vacuum permittivity	Fm^{-1}
ε_r	Relative permittivity	–
μ_0	Vacuum permeability	Hm^{-1}
μ_r	Relative permeability	–
μ_c	Magnetic permeability of conductor	Hm^{-1}
ρ_e	Electric charge density	Cm^{-3}
σ	Electrical conductivity	Sm^{-1}
ω	Angular frequency	$rads^{-1}$
C	Compensation capacitance	F
I	Induction coil current	A
I_{max}	Maximum induction coil current	A
L	Induction coil inductance	H
Q	Quality factor of resonant circuit	–
V	Input voltage	V
	Fluid field	
$C_{1\varepsilon}$	$k-\varepsilon$ turbulence model constant	–
$C_{2\varepsilon}$	$k-\varepsilon$ turbulence model constant	–
C_μ	$k-\varepsilon$ turbulence model constant	–
$c_{p,f}$	Specific heat capacity of fluid	$Jkg^{-1}K^{-1}$
$\mathbf{g}$	Gravitational acceleration vector	ms^{-2}
G_k	Production of turbulent kinetic energy	Wm^{-3} *
k	Turbulent kinetic energy	m^2s^{-2}
k_f	Thermal conductivity of fluid	$Wm^{-1}K^{-1}$
p	Fluid pressure	Pa
$q_{v,f}$	Volumetric heat source in fluid domain	Wm^{-3}
T_f	Fluid temperature	K
t	Time	s
$\mathbf{v}$	Fluid velocity vector	ms^{-1}
v_j	j-direction fluid velocity component	ms^{-1}
x_j	Spatial coordinate in the j-direction	m
ε	Turbulent kinetic energy dissipation rate	m^2s^{-3}
μ	Dynamic viscosity	Pa s
μ_t	Turbulent dynamic viscosity	Pa s
ρ_f	Fluid density	kgm^{-3}
σ_k	Turbulent Prandtl number for k	–
σ_ε	Turbulent Prandtl number for ε	–

T_{in}	Inlet fluid temperature	K
$\mathbf{v}_{in}$	Inlet fluid velocity vector	ms^{-1}
$\mathbf{v}_f$	Fluid velocity vector at the fluid–solid interface	ms^{-1}
	Solid thermal field	
$c_{p,s}$	Specific heat capacity of solid	$Jkg^{-1}K^{-1}$
k_s	Thermal conductivity of solid	$Wm^{-1}K^{-1}$
$q_{v,s}$	Volumetric heat source in solid domain	Wm^{-3}
T_s	Solid temperature	K
ρ_s	Solid density	kgm^{-3}
h	Convective heat-transfer coefficient	$Wm^{-2}K^{-1}$
q''_{conv}	Convective heat flux	Wm^{-2}
q''_{rad}	Radiative heat flux	Wm^{-2}
T_{amb}	Ambient temperature	K
ε_s	Surface emissivity	–
σ_{SB}	Stefan–Boltzmann constant	$Wm^{-2}K^{-4}$
$\mathbf{v}_s$	Solid velocity vector	ms^{-1}
n	Unit normal direction at the fluid–solid interface	–
	Thermal-performance KPIs	
$c_{p,c}$	Specific heat capacity of concrete	$Jkg^{-1}K^{-1}$
m_c	Mass of concrete storage medium	kg
P_{charge}	Charging power of concrete storage medium	W
$P_{\text{discharge}}$	Discharging power of concrete storage medium	W
Q_c	Sensible thermal energy stored/released by concrete	J
$T_{c,\text{avg}}$	Volume-averaged concrete temperature	K
$T_{c,\text{avg},0}$	Initial volume-averaged concrete temperature	K
ΔT_c	Change in volume-averaged concrete temperature	K
Δp	Pressure drop across the CTES module	Pa
p_{inlet}	Inlet pressure	Pa
p_{outlet}	Outlet pressure	Pa
	Abbreviations	
TES	Thermal energy storage	–
CTES	Concrete thermal energy storage	–
DC	Direct current	–
EM	Electromagnetic	–
HTF	Heat-transfer fluid	–
ICFD	Incompressible computational fluid dynamics	–
SHS	Sensible heat storage	–
LHS	Latent heat storage	–
PCM	Phase change material	–
ST	Single-tube configuration	–
MT	Multiple-tube configuration	–
TPMS	Triply periodic minimal surface	–
MER	Mean absolute error	

1. Introduction

Global renewable capacity is projected to rise from 666 GW in 2024 to approximately 935 GW by 2030, with photovoltaic and wind power accounting for 95% of this growth [1]. The growth of renewable energy production may cause supply-and-demand mismatches in the electricity grid due to the less predictable nature of renewable sources, which may strain power grids and require flexible strategies to address them. [2]. Meanwhile, significant amounts of energy are constantly wasted as industrial waste heat in sectors like steel, aluminium, cement, chemicals, and power generation, where much of the thermal energy is released into the environment at low to medium temperatures (<230 °C for low-grade and 230–650 °C for medium-grade waste heat) [3]. The combined issues of renewable energy intermittency and underused industrial waste heat emphasise the increasing need for technologies that can temporarily separate energy supply from demand [4-6].

To address these issues, thermal energy storage (TES) has been developed to convert surplus heat or electricity into stored thermal energy for later use at the end user's location [7]. A TES system comprises three primary components: a power-to-heat module, a heat storage medium (such as molten salt, silica sand, or water), and an energy conversion module that transfers energy into electricity, thermal, or chemical forms [8]. This setup allows for energy arbitrage, improves grid flexibility, and helps shift peak loads by aligning thermal energy requirements with renewable energy availability, usually resulting in reduced costs and improved scalability. In addition, TES methods encompass sensible, latent, and thermochemical heat storage, each characterised by distinct mechanisms, energy densities, heat loss profiles, and applicability [9]. Sensible heat storage (SHS) involves retaining heat in a medium, governed by its specific heat capacity, mass, and temperature differential. It is economically viable and widely utilised; however, it requires large volumes and is prone to heat dissipation over time [10]. Optimising storage density can be achieved with high specific heat capacitiy materials, while high thermal conductivity facilitates efficient charging and discharging processes [11]. Common SHS materials, such as sand, rocks, and concrete, are cost-effective and straightforward, enabling scalability for utility-scale and industrial heat applications, although they inherently require substantial volumetric space [12]. Among them, concrete exhibits a moderate specific heat capacity of 0.88~1.0 kJ/(kg·K) and a wide operating temperature range of 20–500 °C, while maintaining a low material cost of approximately \$0.05~\$0.3 per kg [13]. Its excellent castability and geometric flexibility enable it to be easily moulded or additively manufactured into diverse structural forms and integrated heat exchanger setups.

For concrete thermal energy storage (CTES), efficient heat transfer is vital to the performance of TES systems [13]. The extensive use of steel pipes (Figure 1) and heat transfer fluids may lead to high costs, thereby restricting their economic competitiveness [14]. Techniques to enhance heat transfer include developing concrete mixes with high thermal conductivity [15], optimising the geometry and configuration of the storage medium [16], improving contact between the medium and the concrete, minimising thermal losses with insulation [17], and using enhancements such as fins or heat exchangers [18]. The use of multiple embedded tubes

has also been investigated as an effective approach to enlarge the heat-transfer area and shorten the heat-conduction path within concrete-based TES units, thereby improving the thermal charging and discharging rates [19, 20]. Conventional heat transfer fluid (HTF) structures with straight fins often struggle to meet the requirements of high heat-transfer efficiency, thereby motivating growing interest in advanced heat exchanger geometries [21]. Triply Periodic Minimal Surface (TPMS) structures offer a promising alternative due to their unique geometric and functional characteristics [22]. Their interconnected and nearly isotropic architectures provide high surface-to-volume ratios, enabling efficient thermal management, while the continuous and periodic nature of TPMS structures also leads to favourable hydraulic properties that can enhance overall heat exchanger performance [23]. There has been a wide range of research about the application of TPMS structures in latent heat storage (LHS) [24, 25]. With a relative density of just 10%, the TPMS structure shortened the melting time from 70 minutes for pure phase change materials (PCM) to about 50 minutes [26]. As a heat exchanger for enhanced flow and thermal performance, the Gyroid emerged as the optimal structure under the Nusselt number criterion, significantly outperforming the Diamond structure [27]. The literature has shown that different HTF structures can significantly improve the heat transfer efficiency of the CTES system [28].



Figure 1 Schematic and photographs of the CTES module with embedded HTF channels and an external steel casing [29].

Furthermore, research scholars have investigated alternative heating mechanisms for SHS systems. Unlike the conventional approach in which solar collectors are used to directly heat HTF during the charging of SHS systems, different heating methods, such as resistive heating, microwave heating, ohmic heating and induction heating [30], have been proposed for power-to-heat SHS systems [31]. It has been shown that resistive-heating SHS systems could achieve efficiencies of 85~95% round trip, which are affected by insulation quality and storage material properties [32]. Recent studies have also investigated resistive heating for CTES applications, demonstrating its feasibility for direct electrical charging of solid storage media with relatively simple system integration [33]. The electrically charged system achieved comparable thermal storage behaviour to conventional thermal charging, demonstrating the potential of resistive heating as a relatively simple power-to-heat approach for medium-temperature CTES applications. However, resistive heating is limited by direct heating between a heating element and the heated object and short material lifespan under harsh conditions [8]. On the other hand, electromagnetic (EM) induction heating offers a non-contact process with high heating

efficiency, flexibility, and precise control [34]. In this context, Lu et al. [1] proposed a new type of SHS with moving conductive particles heated with electromagnetic induction. The heat transfer intensity could reach up to 784.6 W/(m^2/K). Ibekwe [35] found that firebricks can be induction-heated to temperatures exceeding 700°C. The rate of temperature increase is directly proportional to electrical conductivity. Liu et al. [36] developed a multi-physical field model for molten-salt induction heating. Increasing the current density could reduce the melting time by up to 51.8%. Zhang et al [37] discovered that using cast iron as the thermal storage and induction heating results in faster initial heating of 8.5 ℃/min and higher storage temperatures of 900 ℃ than traditional resistance devices. The literature on induction heating for SHS shows great potential as a rapid, controllable, volumetric heating method to improve the performance of CTES systems.

Despite existing studies on the induction heating of SHS systems, the comprehensive literature review reveals several research gaps in current studies as follows:

1. Lack of systematic evaluation of induction heating mechanisms in CTES application.
2. Insufficient experimental–numerical coupled validation for induction-heated CTES.
3. Limited understanding of different HTF heat exchange structures, including multiple tubes and TPMS-based configurations, regarding thermal and hydraulic performance under the induction heating method.

This study contributes to the emerging research of induction heating of SHS in the literature through an experimental and multiphysics modelling investigation. To address the identified gaps, this study presents a unified experimental–numerical framework to systematically evaluate the performance of an inductively heated CTES system with different HTF structures. The scientific contribution of this study is as follows:

1. Experimentally compare charging and discharging power, thermal uniformity, and pressure drop characteristics of an inductively heated CTES system with different HTF structure geometries.
2. Develop and validate the numerical, multiphysics modelling of the inductively heated CTES system.
3. Investigate the thermal enhancement potential of various HTF structures via parametric modelling using the validated numerical models.

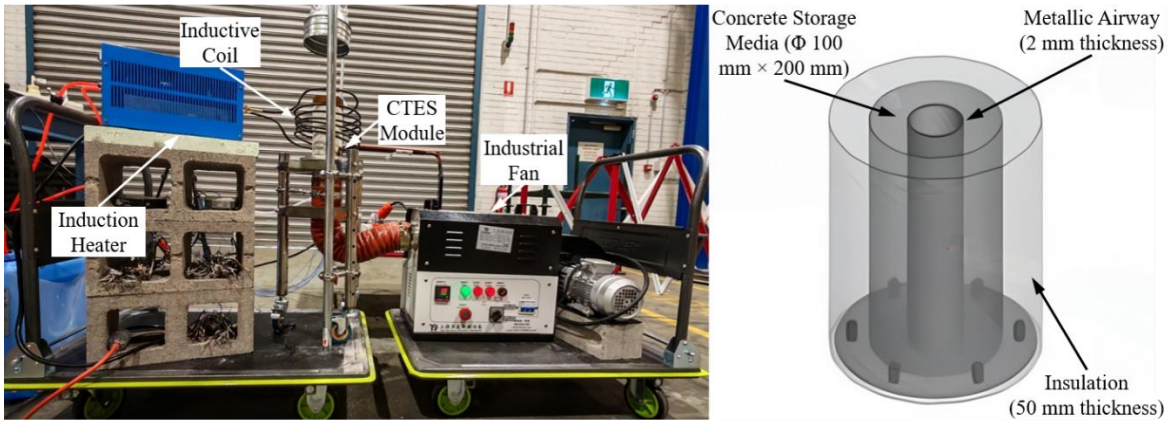
The following section presents the experimental testing. Next, Section 3 describes the development of the multiphysics modelling. Section 4 presents the results and discussion. Finally, Section 5 presents the conclusions and outlook.

2. Experimental Laboratory Testing

Here we summarise details of the experimental program, including the setup on elementary volume testing specimens, the variety of testing undertaken over the different heat exchangers and testing conditions and the key performance indicators used to evaluate results.

2.1 Experimental Setup

To investigate the performance of inductive heating for CTES, a laboratory-scale experimental system was designed to integrate inductive heating and forced air convection for the charging and discharging of the CTES module. The experimental program aims to systematically evaluate the influence of EM -forced air coupling on the behaviour of CTES under controlled conditions. Figure 2 illustrates the experimental setup and the configurations of HTF structures (only the single-tube ST configuration is shown in Figure 2) used for inductive heating in the CTES modules as well as for extracting the stored heat during discharge. Inductive heating is achieved by placing an external induction coil around the CTES module, enabling non-contact volumetric heating of the internal HTF structure. An industrial fan provides forced convection through the HTF during the discharge phase. The CTES module consists of a cylindrical concrete storage medium with a diameter of 100 mm and a height of 200 mm, surrounded by a 50-mm-thick thermal insulation layer to minimise heat loss to the environment. The concrete used in this study was prepared using a commercially available pre-mixed concrete obtained from a local supplier. The compressive strength is 46 MPa, and the density is 2 200 kg/m^3. Samples were cast to measure thermal properties using the Hot Disk TPS 2 500. The thermal conductivity and volumetric heat capacity of concrete are 1.95 W/(m·K) and 863 J/(kg·K), respectively. The insulation material used in this study was AIS STONEWOOL™ 80 BL, a non-combustible mineral wool insulation designed for high-temperature thermal applications (up to a maximum service temperature of 650 °) [38]. The material has a nominal density of 80 kg/m^3 and a low thermal conductivity of 0.032 W/(m·K) at a mean temperature of 23 °C, indicating excellent thermal insulation performance during the experiments.



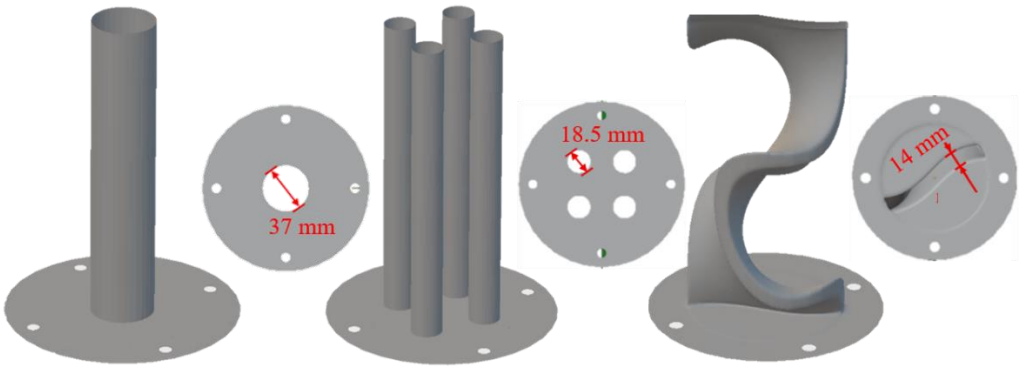
(a) Test setup of the induction-heated CTES system (b) Configuration of CTES module

Figure 2 Experimental setup of the induction-heated CTES system in this study: a) laboratory setup, and b) detail of the CTES module with the ST configuration.

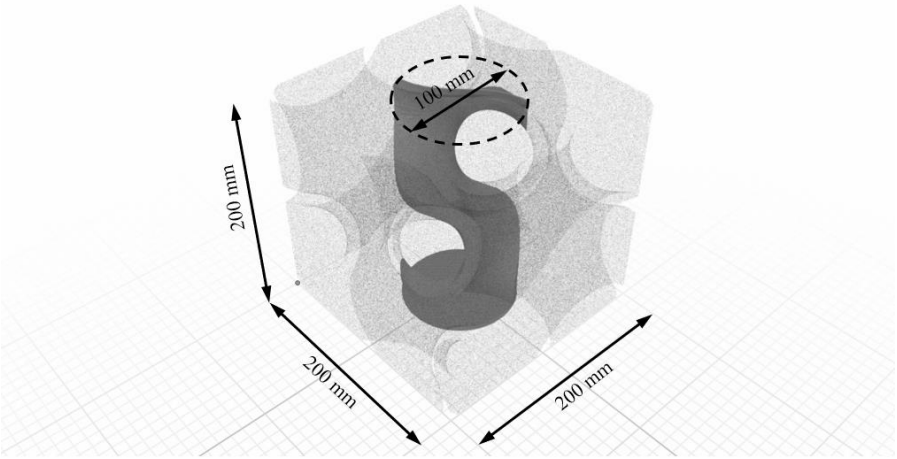
To evaluate the influence of the geometry of HTF structures on the thermal charge and discharge performance of CTES, three different configurations, presented in Figure 2, were considered in this study: a conventional single-tube design (ST), a multiple-tube design (MT), and a TPMS design. The three HTF structures were designed to maintain a constant volume within the CTES module (20% of the total volume), enabling a fair comparison of thermal

storage and heat-transfer behaviours across tests, fabricated by metal additive manufacturing using 18Ni300 maraging steel powder. The powder exhibited a spherical morphology, a particle size range of 15–53 μm, and good flowability, enabling the stable fabrication of complex airway geometries. The material density is taken as 7.88 kg/m^3, with a thermal conductivity of 25.1 W/(m·K) and a specific heat capacity of 377 J/(kg·K). The electrical conductivity is taken as 1.0×10^6 S/m with a relative magnetic permeability of 100 [39].

The ST configuration in Figure 3(a) consists of a single circular metallic tube with a diameter of 37 mm, representing a simplified baseline geometry commonly used in conventional CTES systems. The MT configuration shown in Figure 3(b), employs four parallel circular tubes with a diameter of 18.5 mm to increase the total heat-transfer surface area while maintaining relatively simple flow channels. As depicted in Figure 3(c), the gap distance of the TPMS configuration is set at 14 mm. The detail in Figure 3(d), shows that the TPMS design was generated by extracting a continuous airflow passage from a 200×200×200 mm TPMS unit cell. A cylindrical region with a characteristic diameter of 100 mm was intersected with the periodic TPMS geometry to form a manufacturable internal structure while preserving the characteristic curved topology of the TPMS surface.



(a) Single-tube metallic airway (ST) (b) Multi-tube metallic airway (MT) (c) TPMS metallic airway (TPMS)



(d) Details of the geometry and dimensions of the TPMS airway

Figure 3 Geometric configurations of the metallic airways investigated for the CTES modules: ST (a), MT (b), and TPMS (c) airways, including a detail of the extraction process of the TPMS airway from a periodic TPMS unit cell (d)

2.2 Test Procedure

In this study, the thermal charging phase of the CTES module was achieved by inductive heating, while discharging was realised by forced convection with an external fan to drive airflow through the HTF structure (as shown earlier in Figure 2). During charging, the CTES module was heated by an external water-cooled copper induction coil wrapped around the concrete specimen, as illustrated in Figure 4. The tests used two coil configurations with different diameters. For the ST/MT/TPMS-200 configurations, a 200 mm-diameter coil with seven turns and a pitch of approximately 15 mm was used, resulting in a total coil height of approximately 140 mm. For the ST/MT/TPMS-150 configurations, a 150 mm coil diameter and a corresponding compact winding arrangement were adopted. The coils were positioned at 15 mm from the top of the specimen as shown in Figure 4. The induction heating system was powered by a 55 V direct current (DC) power supply connected to a high-frequency resonant inverter operating at approximately 50 kHz. The charging duration was 90 minutes for the 200 mm coil and 45 minutes for the 150 mm coil, respectively, due to the higher heating efficiency of the 150 mm coil, as discussed later in Section 4. After the charging stage, the induction coil was switched off, and the discharging stage was initiated. During thermal discharging (90 minutes), an industrial fan was activated to induce airflow through the HTF structures, thereby initiating convective heat extraction from the CTES module. The airflow rate was maintained constant (2.6 m/s, 25 °C, 90 min) throughout all discharging tests to ensure consistent boundary conditions and enable direct comparison of thermal discharge performance among different configurations. Table 1 summarises the testing configurations in this study.

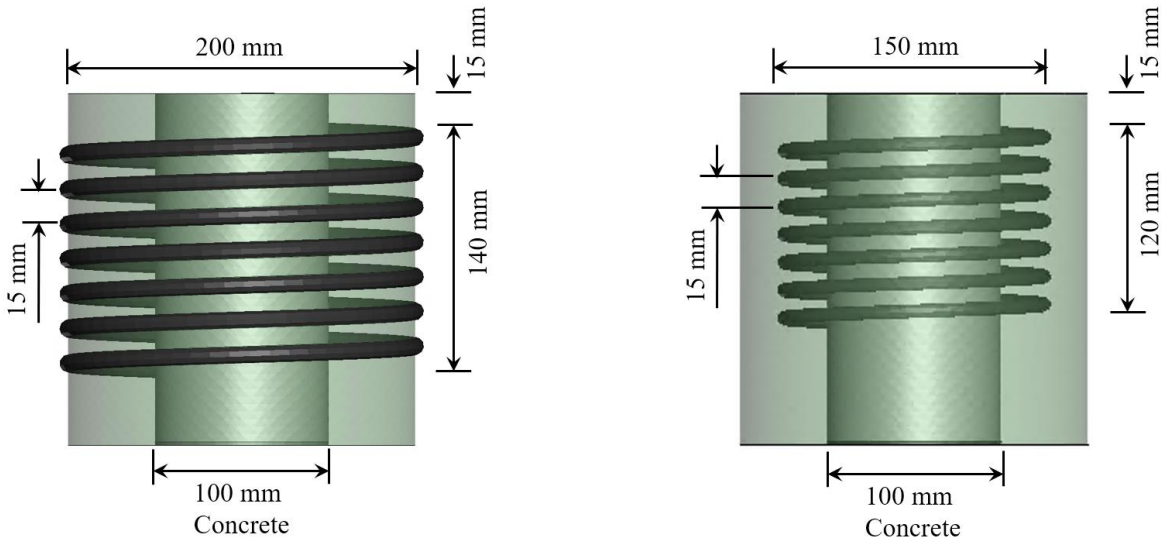


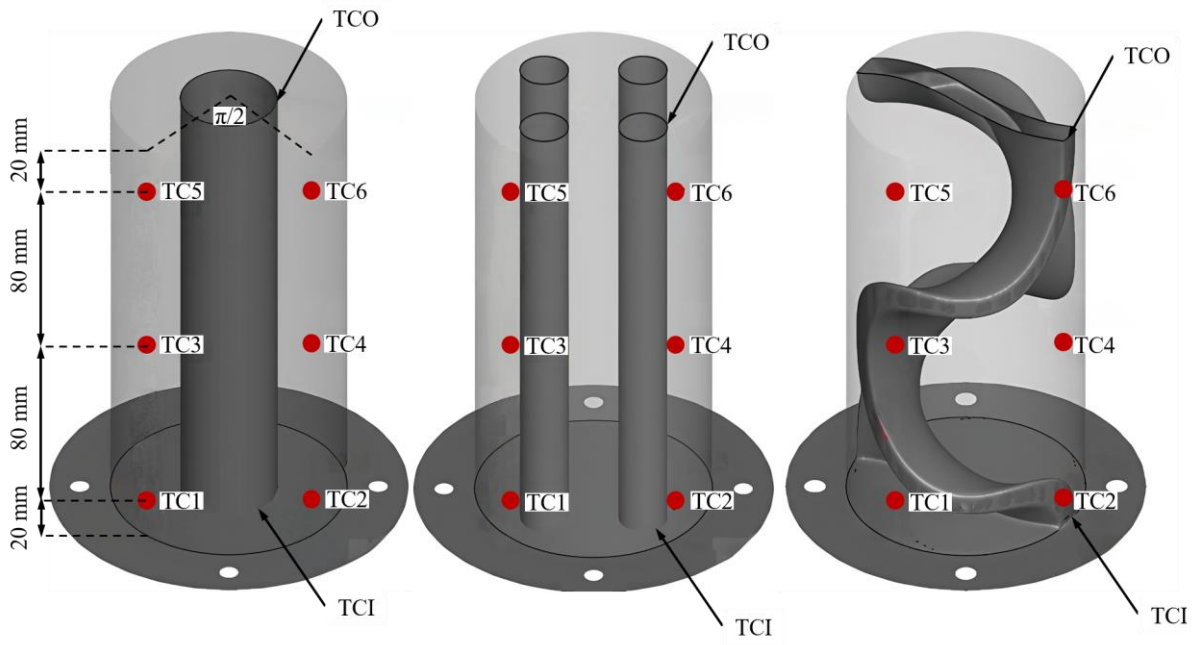
Figure 4 Coil setup for ST/MT/TPMS-200 and ST/MT/TPMS-150

Table 1 Experimental conditions of the CTES system under induction and air heating

Test Group	ST-200	ST-150	MT-200	MT-150	TPMS-200	TPMS-150
Airway Type	Single Tube		Multiple Tube		TPMS	

Thermal Charging	By Induction					
Coil Diameter (mm)	200	150	200	150	200	150
Charging Duration (min)	90	45	90	45	90	45
Voltage (V)	55					
Frequency (kHz)	50					
Thermal Discharging	By Convection					
Inlet Air Temperature (°C)	25					
Inlet Air Velocity (m/s)	2.6					
Discharging Duration (min)	90					

Temperature measurements were continuously recorded during both the thermal charging and discharging stages to monitor the thermal response of the CTES modules. Six surface thermocouples (TC1–TC6) were attached to the outer surface of each CTES specimen to monitor the transient thermal behaviour, as illustrated in Figure 5. TC1 and TC2 were positioned 20 mm above the bottom surface of the specimen, while TC3 and TC4 were located at the mid-height region. TC5 and TC6 were positioned 20 mm below the specimen's top surface. Two thermocouples, denoted TCI and TCO, were installed at the inlet and outlet of the HTF structure, respectively. All CTES configurations used identical thermocouple layouts, regardless of the HTF structure geometry. To further capture the spatial temperature distribution, infrared (IR) thermography is employed, offering qualitative and semi-quantitative insights into surface temperature uniformity and heat propagation characteristics. In addition, a differential pressure sensor (PS, SLD-PTG, Nanjing Shunlaida Measurement and Control Equipment Co., Ltd., China, ±0.1 Pa) was also installed along the inlet airflow pipe to monitor the pressure drop across the CTES module during the discharging stage. Atmospheric pressure is assumed at the CTES module outlet.



(a) ST (b) MT (c) TPMS

Figure 5 Thermocouple layout for CTES modules with different metallic airway configurations

2.3 Performance Indicators

The key performance indicators (KPIs) described below were used to evaluate the performance of the storage systems for the CTES module. Several KPIs, listed and defined in Table 2, have been investigated to analyse the thermodynamic performance of the CTES and to compare the different cases.

Table 2 Key performance indicators for this study

KPI	Definition	Unit	Eq.
Energy Storage Capacity [40]	$Q_c = m_c c_p \lvert T_{c,avg} - T_{c,avg,0} \rvert$	kJ	(1)
Charging Power [41]	$P_{charge} = m_c c_p \frac{dT_{c,avg}}{dt}$	W	(2)
Discharging Power [41]	$P_{discharge} = m_c c_p \frac{-dT_{c,avg}}{dt}$	W	(3)
Charging Time [42]	Time for the $T_{c,avg}$ to increase by 30 °C	min	(4)
Discharging Time [42]	Time for the $T_{c,avg}$ to decrease by 30 °C	min	(5)
Pressure Drop	$\Delta P = P_{inlet} - P_{atm}$	Pa	(6)

* Qc is the energy storage capacity; m_c is the mass of the storage medium; c_p is the specific heat capacity; $T_{c,\mathrm{avg}}$ is the average temperature of the storage medium; $T_{c,\mathrm{avg},0}$ is its initial average temperature; P_{charge} and $P_{\mathrm{discharge}}$ are the charging and discharging powers; ΔP is the pressure drop between the inlet and atmospheric pressure.

3. Multiphysics Modelling

To complement the experimental investigation and provide insight into the underlying physical mechanisms, a multiphysics numerical model was developed to simulate the charging and discharging processes of the CTES modules. The simulations were conducted using LS-DYNA [43], which enables coupled electromagnetic–thermal–fluid analyses. Inductive heating was modelled by solving Maxwell's equations under the eddy-current approximation, capturing the induced currents and associated Joule heating within the metallic HTF structure. The resulting volumetric heat generation was then coupled to the thermal solver to predict heat transfer within the HTF structure, surrounding concrete, and insulation. Convective heat extraction during the discharging stage was modelled using the incompressible fluid dynamics (ICFD) solver in LS-DYNA. In this study, air was modelled as an incompressible fluid with fixed thermo-physical properties. This approach is common in low-Mach-number thermal-fluid simulations, where density changes have little effect on the flow but can greatly increase the computational load [44, 45]. This selection of modelling approach is to enhance numerical stability and compatibility and lower computational demands, particularly in large-scale three-dimensional multiphysics simulations in this study. Accordingly, the air properties were fixed at 299 K as the inlet temperature, with a density of 1.293 kg/m^3, dynamic viscosity of 1.72×10^{-5} Pa/s, thermal conductivity of 0.024 W/(m·K), and specific heat of 1005 J/(kg·K). Finally, heat conduction was employed to model heat transfer within the solid concrete domain of the CTES module.

3.1 Governing Equations

The proposed CTES system was modelled using a coupled electromagnetic–fluid–thermal framework. During charging, the electromagnetic solver was employed to resolve the time-varying electromagnetic field generated by the induction coil and the resulting eddy-current distribution within the electrically conductive components. The induced currents generate volumetric Joule heating, which is subsequently transferred to the thermal solver as an internal heat source. During discharging, the ICFD solver was used to resolve the forced airflow and conjugate heat transfer between the fluid and solid domains. The governing equations adopted for the coupled multiphysics model are summarised in Table 3.

Table 3 Governing equations for the coupled electromagnetic–fluid–thermal model

Physics	Governing relation	Definition	Eq.
Electromagnetic	Ampère–Maxwell law	$\nabla \times \mathbf{H} = \mathbf{J} + \frac{\partial \mathbf{D}}{\partial t}$	(7)
	Faraday's law	$\nabla \times \mathbf{E} = -\frac{\partial \mathbf{B}}{\partial t}$	(8)

	Gauss's law	$\nabla \cdot \mathbf{D} = \rho_e$	(9)
	Gauss's law for magnetism	$\nabla \cdot \mathbf{B} = 0$	(10)
	Electric constitutive relation	$\mathbf{D} = \varepsilon_0 \varepsilon_r \mathbf{E}$	(11)
	Magnetic constitutive relation	$\mathbf{B} = \mu_0 \mu_r \mathbf{H}$	(12)
	Ohm's law	$\mathbf{J} = \sigma \mathbf{E}$	(13)
	Skin depth	$\delta = \sqrt{\frac{2}{\omega \mu_c \sigma}} = \frac{1}{\sqrt{\pi f \mu_c \sigma}}$	(14)
	Joule heat generation	$q_{v,s} = q_J = \mathbf{J} \cdot \mathbf{E} = \frac{\mathbf{J} \cdot \mathbf{J}}{\sigma}$	(15)
Fluid	Mass conservation	$\frac{\partial \rho_f}{\partial t} + \nabla \cdot (\rho_f \mathbf{v}) = 0$	(16)
	Incompressible continuity	$\nabla \cdot \mathbf{v} = 0$	(17)
	Momentum conservation	$\rho_f \left[\frac{\partial \mathbf{v}}{\partial t} + (\mathbf{v} \cdot \nabla)\mathbf{v}\right] = -\nabla p + \rho_f \mathbf{g} + \mu \nabla^2 \mathbf{v}$	(18)
	Turbulent kinetic energy	$\rho_f \left(\frac{\partial k}{\partial t} + v_j \frac{\partial k}{\partial x_j}\right) = \frac{\partial}{\partial x_j}\left[\left(\mu + \frac{\mu_t}{\sigma_k}\right)\frac{\partial k}{\partial x_j}\right] + G_k - \rho_f \varepsilon$	(19)
	Turbulent dissipation rate	$\rho_f \left(\frac{\partial \varepsilon}{\partial t} + v_j \frac{\partial \varepsilon}{\partial x_j}\right) = \frac{\partial}{\partial x_j}\left[\left(\mu + \frac{\mu_t}{\sigma_\varepsilon}\right)\frac{\partial \varepsilon}{\partial x_j}\right] + C_{1\varepsilon}\frac{\varepsilon}{k}G_k - C_{2\varepsilon}\rho_f \frac{\varepsilon^2}{k}$	(20)
	Turbulent viscosity	$\mu_t = \rho_f C_\mu \frac{k^2}{\varepsilon}$	(21)

	Fluid energy conservation	$\rho_f c_{p,f} \frac{\partial T_f}{\partial t} + \rho_f c_{p,f} \mathbf{v} \cdot \nabla T_f = \nabla \cdot \left(k_f \nabla T_f\right) + q_{v,f}$	(22)
Thermal	Solid heat conduction	$\rho_s c_{p,s} \frac{\partial T_s}{\partial t} = \nabla \cdot (k_s \nabla T_s) + q_{v,s}$	(23)

* $\boldsymbol{E}$ is the electric field intensity; $\boldsymbol{H}$is the magnetic field intensity; $\boldsymbol{D}$is the electric flux density; $\boldsymbol{B}$is the magnetic flux density; $\boldsymbol{J}$ is the current density; ρ_e is the electric charge density; σ is the electrical conductivity; $\varepsilon_0$and $\varepsilon_r$are the vacuum and relative permittivities; $\mu_0$and $\mu_r$are the vacuum and relative permeabilities; $\delta$is the skin depth; $f$is the excitation frequency; $q_J$is the volumetric Joule heat generation; ρ_f, $c_{p,f}$, k_f, μ, and $\mu_t$denote the fluid density, specific heat capacity, thermal conductivity, dynamic viscosity, and turbulent viscosity; $\boldsymbol{v}$is the fluid velocity; p is the pressure; $k$is the turbulent kinetic energy; ε is the turbulent dissipation rate; ρ_s, $c_{p,s}$, k_s, and $T_s$denote the density, specific heat capacity, thermal conductivity, and temperature of the solid; $T_f$is the fluid temperature and $q_{v,f}$and $q_{v,s}$are the volumetric heat-source terms in the fluid and solid domains.

The electromagnetic formulation is based on Maxwell's equations [46] together with the corresponding constitutive relations. In the present model, the alternating current supplied to the induction coil generates a time-varying magnetic field, which induces eddy currents within the electrically conductive components. The electromagnetic solution therefore provides the spatial and temporal distributions of the electromagnetic field and induced current density required to determine the corresponding Joule heat generation [47].

At the operating frequencies considered in this study, the induced current distribution is affected by the skin effect, whereby the current density is concentrated near the conductor surface and decreases with penetration depth [48]. The characteristic penetration distance is represented by the skin depth, defined as the depth at which the current density decreases to 1/e (approximately 36.8%) of its surface value. In the numerical model, the skin effect arises from the electromagnetic field solution rather than being imposed as an independent empirical condition. The calculated skin depth provides a physical measure of the penetration of the induced current into the conductive components.

To simulate the fluid (air) behaviour during the discharge stage of the proposed CTES system, the ICFD solver [49] is employed. During discharge, the complex TPMS geometry produces strongly three-dimensional flow passages with substantial local variations in velocity and flow recirculation. Similar thermo-hydraulic behaviour in TPMS structures has been reported by Kwasi-Effah et al. [50], who employed the turbulence model to represent the associated turbulent flow and heat-transfer characteristics. Accordingly, the same turbulence modelling framework was adopted in the present study to resolve the thermo-hydraulic behaviour of the TPMS-based CTES system, with the model formulation following the work by Panchal et al. [51].

Heat transfer within the fluid domain is governed by energy conservation, accounting for transient thermal storage, convective transport by the airflow, and thermal diffusion [52]. No internal volumetric heat source is prescribed within the fluid domain. Within the solid domains, including the concrete storage medium and insulation, heat transfer is represented by transient

heat conduction based on Fourier's law. During induction charging, the volumetric Joule heat from the electromagnetic solution is applied to the electrically conductive solid components, heating the conductive regions. Specifically, the Joule heat q_J, defined in Eq. (15), is introduced as the volumetric heat-source term $q_{v,s}$ in the solid energy conservation equation, Eq. (23). This provides the coupling between the electromagnetic and thermal fields [53].

3.2 Boundary Condition

The boundary conditions applied in the coupled multiphysics model are summarised in Table 4 and illustrated schematically in Figure 6. They comprise the electromagnetic excitation of the induction coil, heat loss from the external surfaces, airflow conditions at the inlet and outlet, and thermal coupling between the fluid and solid domains. For each boundary condition, the corresponding mathematical formulation and its physical role in the coupled model are provided below.

Table 4 Summary of boundary conditions applied in the coupled multiphysics model

Boundary condition	Physical description	Definition	Eq.
Electromagnetic excitation	A sinusoidal current in the induction coil produces an alternating magnetic field, inducing eddy currents in conductive parts that generate Joule heat, which then couples to the thermal model.	$I(t) = I_{\max} \sin(2\pi f t)$	(24)
Radiation	Radiative heat loss occurs between the exposed external surfaces of the solid and the ambient environment.	$q''_{\text{rad}} = \varepsilon_s \sigma_{SB} (T_s^4 - T_{amb}^4)$	(25)
Convection	Convective heat loss from the external surfaces to ambient air is represented using an effective heat-transfer coefficient.	$q''_{\text{conv}} = h(T_s - T_{amb})$	(26)
Air inlet	A prescribed inlet velocity of $2.6\ \text{ms}^{-1}$ and inlet air temperature of $25\ ^\circ\text{C}$ are imposed during the discharge stage.	$v = v_{in}$ $T = T_{in}$	(27)
Air outlet	A pressure outlet is prescribed at the downstream boundary to allow air to leave the computational domain.	$p = p_{\text{out}}$	(28)

Fluid–solid interface: velocity	Velocity continuity is imposed at the fluid–solid interface. For the stationary solid domain, $\mathbf{v}_s = 0$, corresponding to the no-slip condition at the solid surface.	$\mathbf{v}_f = \mathbf{v}_s$	(29)
Fluid–solid interface: heat flux	Heat-flux continuity is enforced across the fluid–solid interface to couple heat conduction in the solid with convective heat transfer in the airflow domain.	$-k_s \frac{\partial T_s}{\partial n} = -k_f \frac{\partial T_f}{\partial n}$	(30)

* $I(t)$ is the instantaneous coil current; $I_{\max}$ is the maximum coil current; f is the excitation frequency; t is time; ε_s is the surface emissivity; σ_{SB} is the Stefan–Boltzmann constant; T_s is the solid-surface temperature; T_{amb} is the ambient temperature; h is the convective heat-transfer coefficient; v_{in} and T_{in} are the prescribed inlet air velocity and temperature; p_{out} is the prescribed outlet pressure; v_f and v_s denote the fluid and solid velocities at the fluid–solid interface; n denotes the outward unit normal direction at the interface.

In this study, the induction heating system is powered by a DC source with a measured input voltage of 55 V during the induction thermal charging stage. A zero-voltage switching inverter converts the DC power supply into a high-frequency alternating current. The inverter drives a resonant inductor–capacitor (LC) circuit formed by the induction coil and the compensation capacitor. At resonance, reactive energy oscillates between the inductance and capacitance, significantly amplifying the circulating current. The inverter converts the DC input into a high-frequency (f = 50 kHz) alternating current, forming a resonant LC circuit consisting of the induction coil (inductance L) and the compensation capacitor (C = 4 μF). The resonant frequency is given by:

$$f = \frac{1}{2\pi\sqrt{LC}} \tag{31}$$

Therefore, the coil inductance is calculated as L = 2.7 μH. In the LC circuit, the circulating current in the induction coil can be estimated as:

$$I_{max} = Q \cdot V \cdot \sqrt{\frac{C}{L}} \tag{32}$$

where Q is the quality factor of the resonant circuit and V is the input voltage applied to the inverter. Using the parameters reported in the literature [54] , the effective quality factor Q can be calculated in the range of [1.7-2] in this study. Therefore, the maximum current in the induction coil is calculated as 110 A for ST/MT/TPMS-200 and 130 A for ST/MT/TPMS-150. The sensitivity of the numerical predictions to variations in the prescribed coil current, together with the selection of these representative current values, is further examined in Section 4.2.

During the thermal discharge stage, the air inlet was prescribed with a velocity of 2.6 m/s and a temperature of 25 °C, while a zero-gauge-pressure condition was imposed at the outlet. At the fluid–solid interfaces, velocity and heat-flux continuity were enforced to represent the conjugate heat transfer between the airflow and the HTF structure. Heat loss from all exposed external surfaces was represented by combined radiation and natural convection. The ambient temperature of 20 °C is used, and the surface emissivity ε_s of 0.8 with a convective heat transfer coefficient h of 8 W/(m^2·K) [55] were adopted.

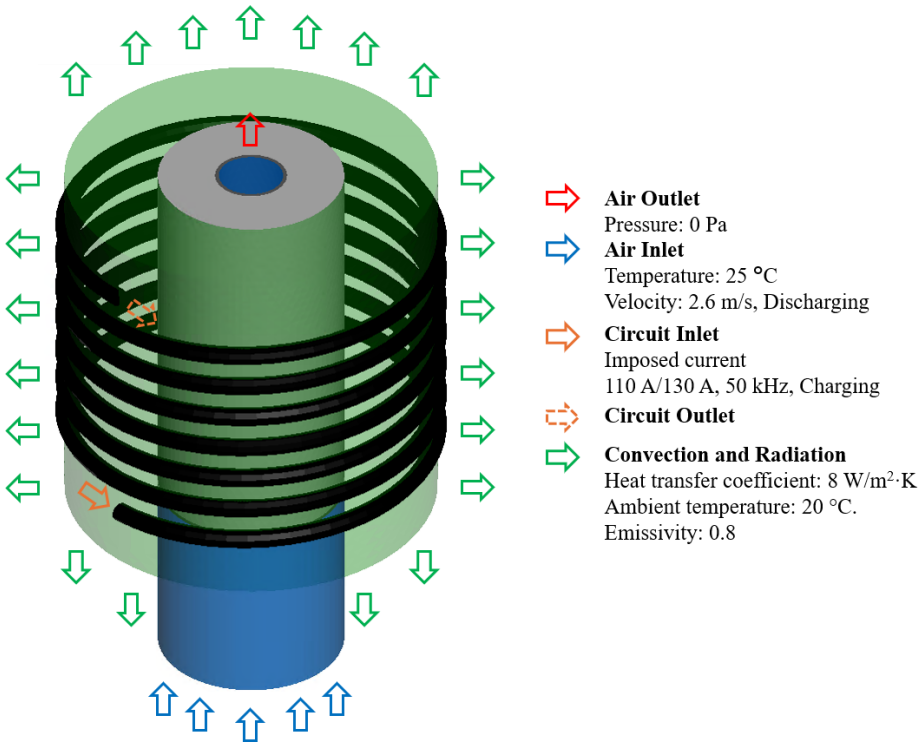


Figure 6 Schematic illustration of the boundary conditions applied in the coupled electromagnetic–thermal–fluid simulation, including induction heating, airflow inlet/outlet, and external convection–radiation heat loss conditions

3.3 Modelling Techniques

The multiphysics simulations in this study involve complex coupling of EM fields, fluid behaviour, and heat transfer, requiring advanced modelling techniques to address numerical challenges. The LS-DYNA induction heating module heats metallic HTF structures by EM induction, generating eddy currents within the HTF structures and subsequently Joule heating. The module solver works in the time domain and requires a very small time step, compatible with the frequency, to solve the eddy current problem [56]. To address this issue, the inductive heating solver implemented in LS-DYNA employs separate electromagnetic “micro” and “macro” time scales (Figure 7). These averages are then used in a larger time step in the thermal solver (EM “Macro” time step), assuming material properties stay constant within this interval [57].

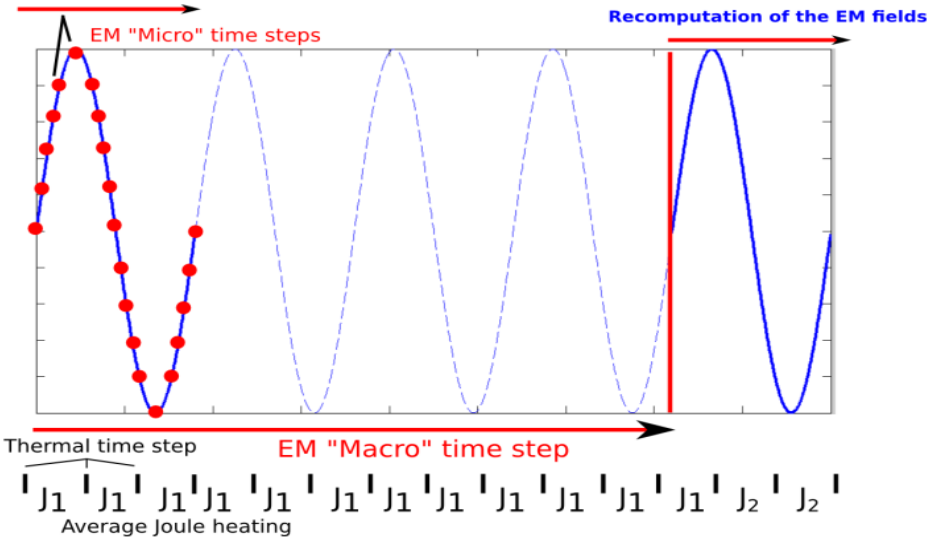


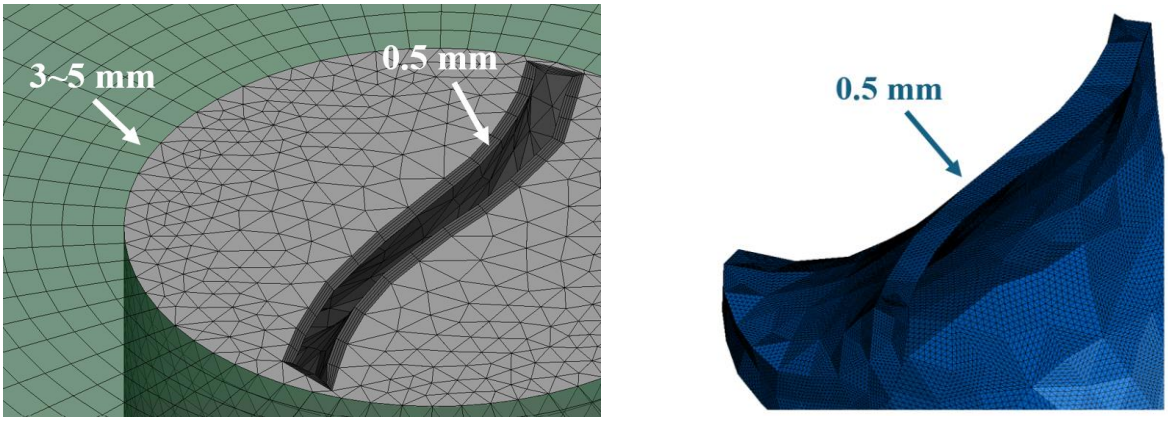
Figure 7 Schematic illustration of the micro- and macro-time-step strategy used in the LS-DYNA electromagnetic solver for inductive heating simulations [56]

As temperature evolves and material properties change, the EM solution is periodically updated by re-solving the eddy current problem over another full cycle to obtain new averaged values. In addition, a sequential coupling strategy was used to improve efficiency and stability by decoupling the EM charging step and the forced-air convective discharging step. The EM solver calculated the volumetric Joule heating generated in the conductive components, which was subsequently used as the heat source in the solid energy equation to obtain the transient temperature field during the charging stage. The final temperature was then used as the initial condition for the next discharge-stage analysis, in which the coupled thermodynamic response of the airflow field and heat transfer in the solid domain were resolved using the ICFD solver. The EM induction solver was deactivated in the discharge stage, and vice versa.

A timestep convergence study indicated that 50 EM micro time steps per excitation-current period were sufficient to resolve the high-frequency electromagnetic response and the associated Joule heating. In the LS-DYNA inductive-heating solver, the electromagnetic field is resolved over the current period using these micro time steps, from which the average Joule heating is calculated and transferred to the thermal solver. The electromagnetic field and Joule-heating source are subsequently updated at each EM macro time step. An EM macro time step of 1 s was adopted in this study, providing stable and converged temperature predictions while substantially reducing the computational cost. For the ICFD simulation during the discharging stage, a smaller time step of 0.001 s was employed to capture the transient airflow behaviour and maintain numerical stability.

In addition, Figure 8 illustrates the computational meshes used for the coupled electromagnetic–thermal–fluid simulations in this study. Separate solid and fluid domains were generated to accurately capture heat transfer within the concrete storage medium and airflow behaviour inside the HTF structures. For the solid domain, an unstructured tetrahedral mesh was employed for both the concrete and metallic airway regions to accommodate the complex TPMS geometry and curved interfaces. A locally refined mesh with a minimum element size

of approximately 0.5 mm was applied near the HTF surfaces to accurately resolve the steep thermal gradients and electromagnetic-induced heat generation during induction charging. In contrast, a coarser mesh size of approximately 3–5 mm was adopted in the bulk concrete region to reduce computational cost while maintaining sufficient thermal accuracy. For the fluid domain, a dedicated high-resolution mesh was used to capture airflow development, local velocity gradients, and convective heat transfer during discharge. Similar local refinement near the airway wall was used to improve predictions of wall heat transfer and fluid–solid thermal interaction.



(a) Solid Domain (b) Fluid Domain

Figure 8 Computational meshes of the solid and fluid (air) domains in the coupled multiphysics model in this study

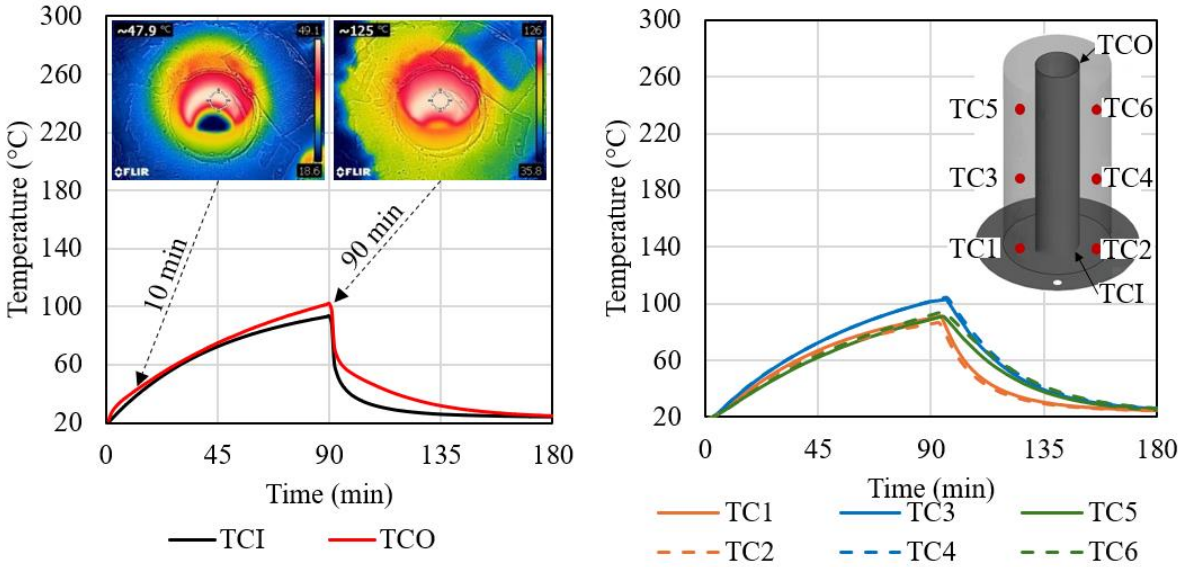
4. Results and Discussion

This section presents an integrated performance evaluation and comparative analysis of the proposed CTES system through comprehensive experimental measurements and numerical results. First, the thermal behaviour of the CTES module is experimentally characterised using embedded thermocouples distributed along the axial direction of the storage domain, providing time-resolved temperature evolution and pressure drop development for each configuration (Section 4.1). In addition to thermal performance, the system's hydraulic response is assessed through pressure-drop measurements during the discharge stage. The developed multiphysics model is validated in Section 4.3 and used for parametric modelling in Section 4.4.

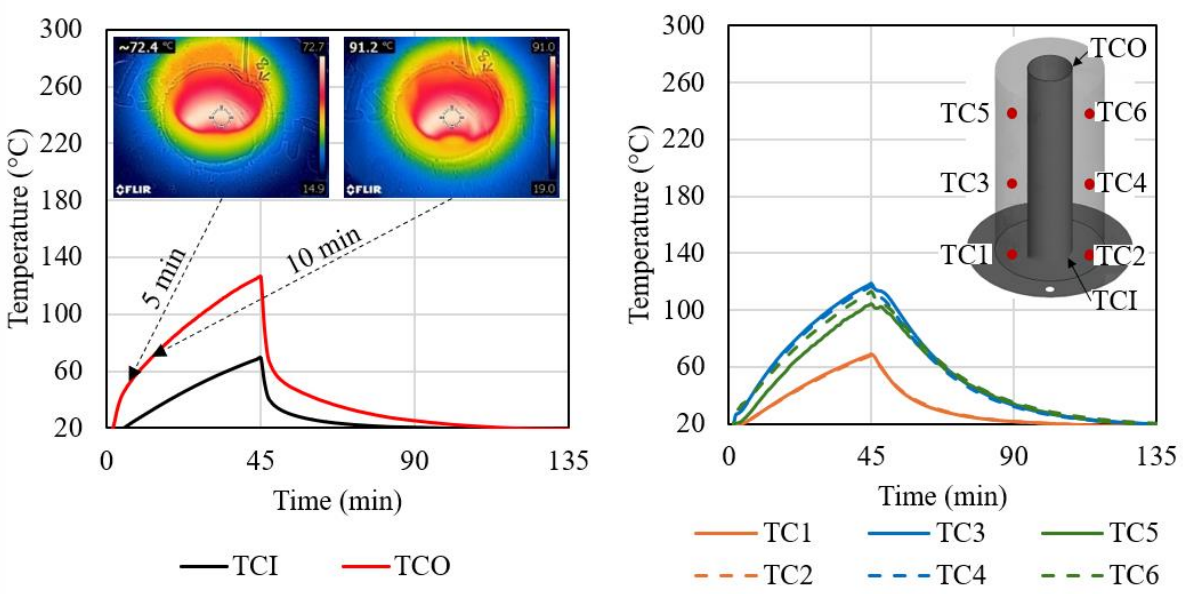
4.1 Experimental Results

Figure 9 presents the temperature responses of the proposed CTES system during charging and discharging. For all tested configurations, the inlet temperature (TCI) increased progressively during charging and dropped sharply upon switching to discharging, clearly indicating the transition between the two operating modes. Good agreement was generally observed between the thermocouple measurements and the infrared thermal images, suggesting that the measured temperature evolution reliably reflected the thermal behaviour of the specimens. A notable feature of the induction-heating process was the relatively uniform temperature rise throughout

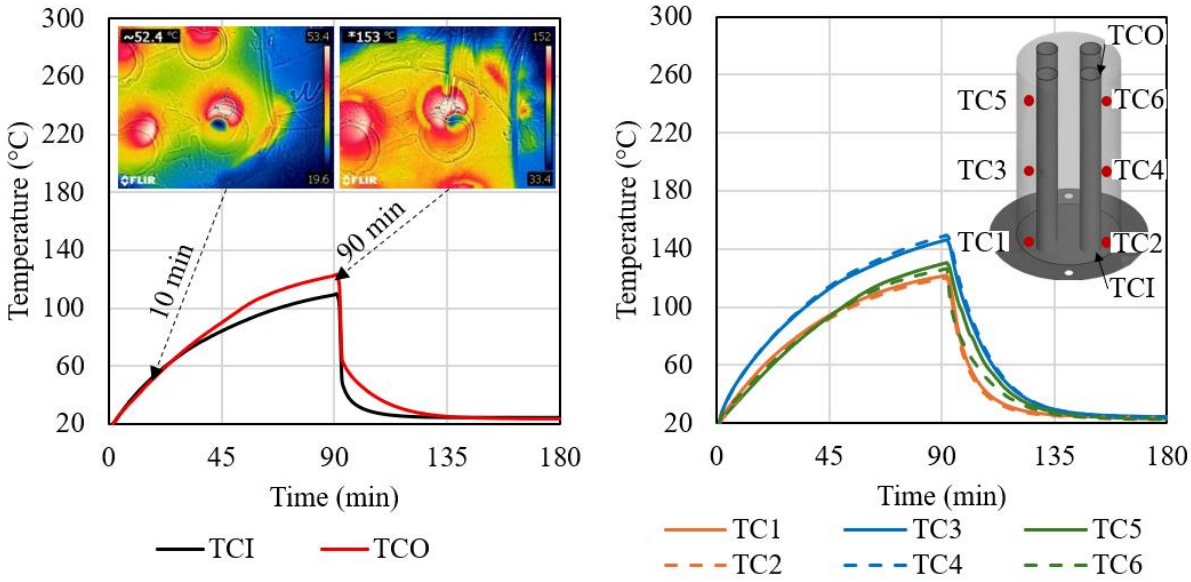
the specimen during charging, particularly for the ST-200 and MT-200 cases, where the temperature differences among TC1–TC6 remained comparatively small. The experimental results further demonstrate that the heating response strongly depends on coil diameter and metallic-airway configuration. Reducing the coil diameter from 200 to 150 mm substantially intensified the electromagnetic interaction and resulted in considerably higher specimen temperatures within the same charging period; for example, the 150 mm configurations reached markedly higher temperatures after 45 min than their corresponding 200 mm cases. This sensitivity to coil geometry provides additional design flexibility, as heating intensity and spatial distribution can be tailored by optimising the coil and internal metallic structure. The results demonstrate that electromagnetic induction heating offers a promising route toward rapid and volumetrically distributed charging of concrete thermal energy storage systems, while also providing substantial flexibility for thermal-performance optimisation.



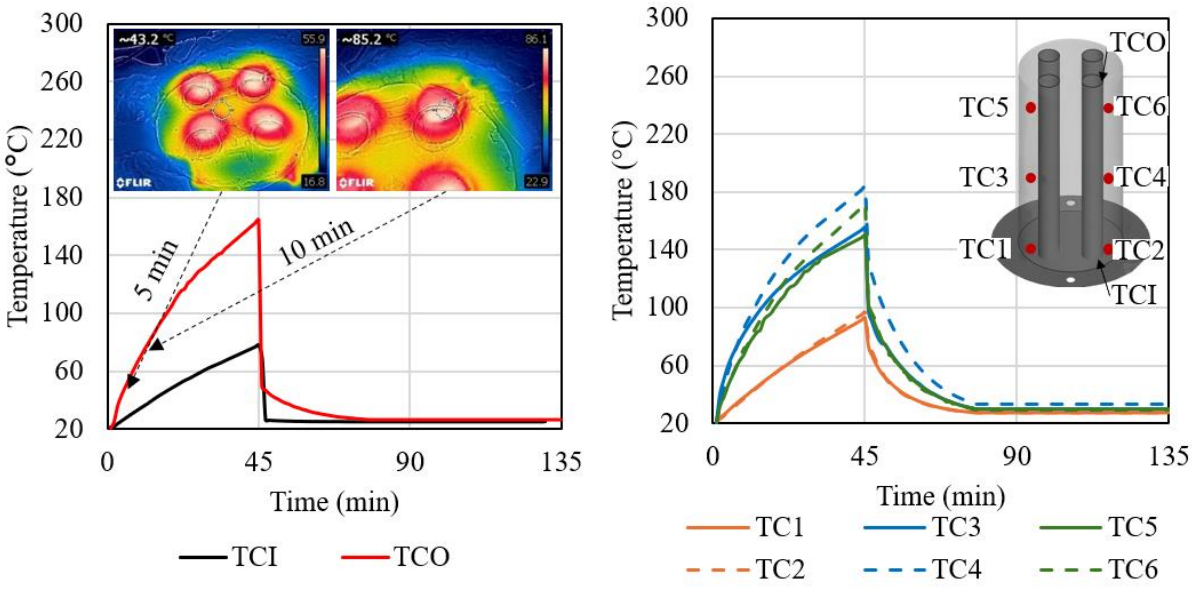
a) ST-200 configuration



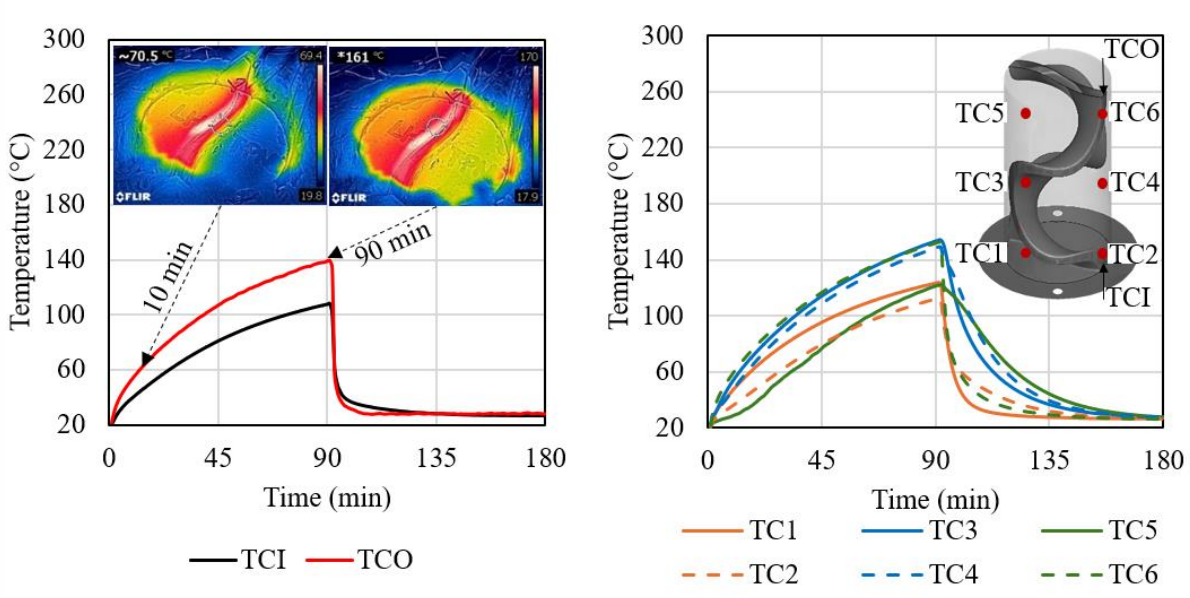
b) ST-150 configuration



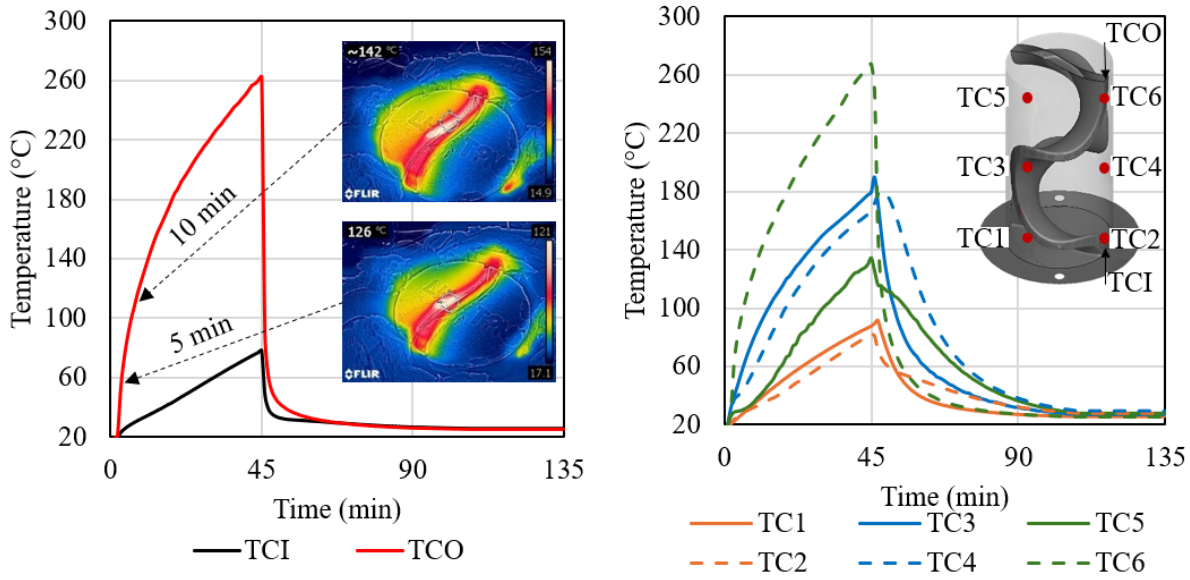
c) MT-200 configuration



d) MT-150 configuration



e) TPMS-200 configuration



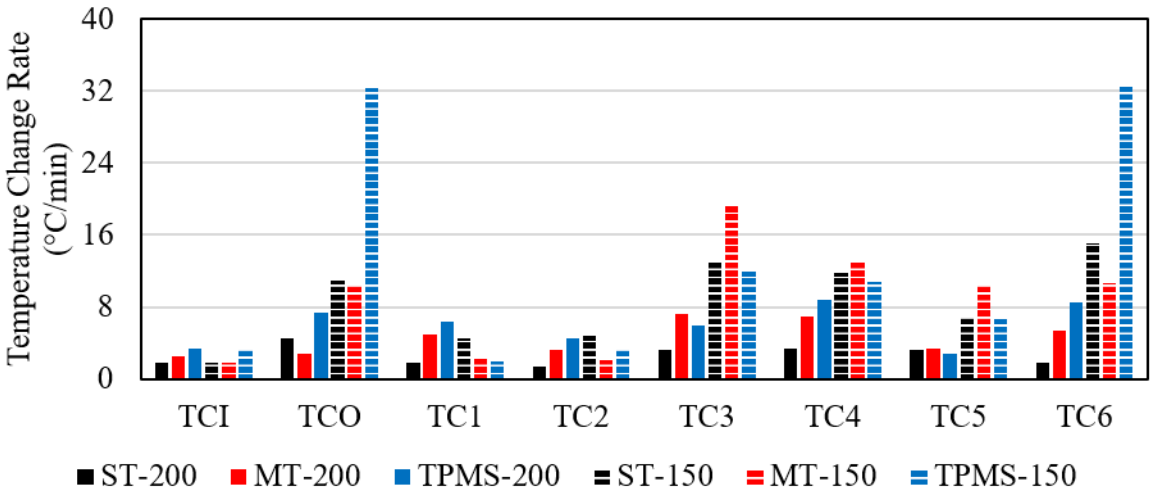
f) TPMS-150 configuration

Figure 9 Thermal responses for ST, MT, and TPMS configurations with 200/150 mm coil.

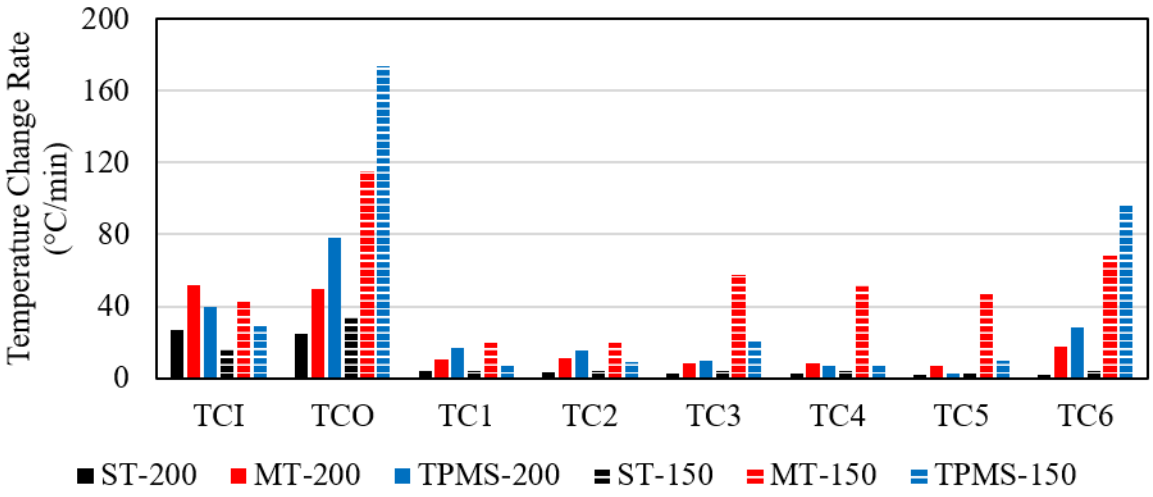
Figure 10 quantitatively compares the maximum 1-min temperature change rates during charging and discharging for all configurations. For the 200 mm specimens, both the MT and TPMS designs generally produced substantially faster thermal responses than ST-200. Considering TC1–TC6 collectively, the mean of the maximum charging rates increased from approximately 2.49 °C/min for ST-200 to 5.2 °C/min for MT-200 and 6.2 °C/min for TPMS-200, corresponding to improvements of about 108% and 147%, respectively. The enhancement was even more pronounced during discharging, for which the corresponding mean maximum rates increased from 2.8 °C/min to 10.5 and 13.3 °C/min, representing increases of approximately 272% and 368%. At individual locations, the improvement could be

considerably greater; for example, at TC4 the maximum charging rate increased from 3.4 °C/min for ST-200 to 6.9 °C/min for MT-200 and 8.8 °C/min for TPMS-200, while at TC6 the maximum discharging rate increased from 1.8 °C/min to 17.5 and 28.1 °C/min, respectively.

The results indicate that the embedded metallic and TPMS structures improve the effectiveness of induction heating by extending the electromagnetically heated region into the concrete domain and facilitating subsequent heat conduction from the metallic network to the surrounding concrete. This reduces dependence on the proximity of the external coil and promotes a faster, more spatially distributed thermal response. From an engineering perspective, the MT configuration provides a particularly attractive balance between thermal performance and manufacturability. Despite its relatively simple geometry, MT-150 achieves charging and discharging rates comparable to, and in some cases exceeding, those of the more geometrically complex TPMS configurations. More importantly, the results show that the internal inductively heated structures can partly compensate for the weaker electromagnetic coupling associated with the larger 200 mm coil, allowing the enhanced 200 mm configurations to approach, and at some locations exceed, the thermal response observed for the smaller 150 mm specimens. At the reduced coil size (150 mm), all configurations exhibit accelerated temperature evolution due to the improved electromagnetic coupling associated with the smaller coil diameter. The TPMS-150 specimen achieves the highest heating rate, reflecting the combined effects of a reduced coil-to-structure distance and an enlarged conductive heat-transfer pathway.



(a) Thermal charging



(b) Thermal discharging

Figure 10 Maximum temperature change rates measured at the inlet, outlet, and internal thermocouple locations for all configurations during (a) charging and (b) discharging.

Compared with ST, the MT configuration exhibits a more distributed temperature rise along the specimen height, reflecting the presence of multiple metallic airways that act as spatially distributed induction-heating elements. This arrangement promotes heat generation at multiple locations within the specimen and facilitates subsequent heat diffusion into the surrounding concrete. TPMS produces the highest overall heating rates; its temperature distribution is less uniform, with more pronounced temperature differences among the thermocouple locations. This behaviour is associated with the continuous TPMS geometry, which extends further toward the outer region of the specimen and therefore places portions of the metallic structure closer to the induction coil. The reduced coil-to-metal distance can locally enhance electromagnetic interaction and eddy-current generation, leading to more intensive heating in these regions [58]. Consequently, TPMS provides a stronger local induction-heating response, whereas MT tends to distribute the induced heat generation more evenly throughout the specimen. These observations are consistent with the thermocouple measurements and demonstrate that the geometry and spatial location of the metallic airway govern not only the magnitude of induction heating but also the distribution of heat generation within the concrete specimen.

The pressure drop remains relatively stable for all three configurations throughout the discharging period, indicating a steady flow regime (Figure 11). However, clear differences in magnitude are evident. The TPMS configuration consistently exhibits the highest pressure drop (≈480–510 Pa), followed by MT (≈310–330 Pa), while ST shows the lowest values (≈260–290 Pa). This trend suggests that the TPMS structure introduces greater flow resistance, likely due to its more complex geometry, increased surface area, and enhanced flow tortuosity; which conversely enhances heat transfer. In contrast, the simpler ST structure allows smoother airflow with reduced frictional losses. Minor differences are observed between the 200 and 150 mm coil tests for the same configuration, likely due to experimental variability rather than

systematic effects, since the internal flow geometry remains unchanged. The higher pressure drop of TPMS and, to a lesser extent, MT reflects increased flow resistance from their complex internal geometries, larger surface areas, and flow tortuosity. This aligns with previous studies showing that complex heat-transfer structures with more area and flow disturbance generally have higher pressure losses. Conversely, the simpler, more open flow path of the ST configuration results in lower frictional resistance.

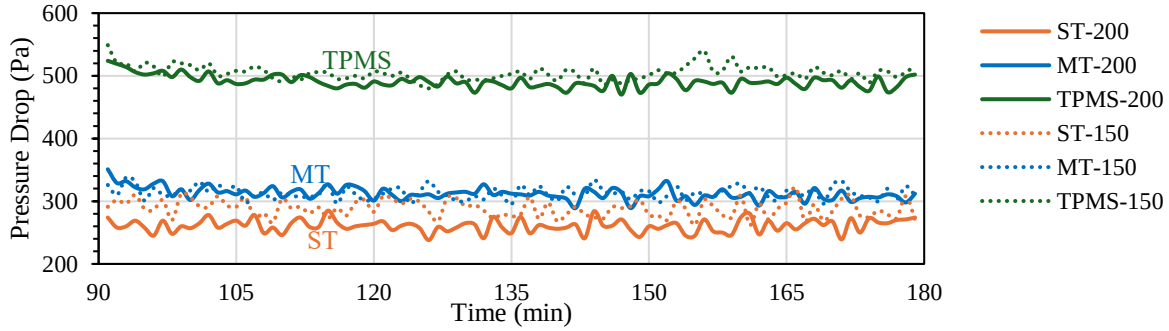


Figure 11 Pressure drop comparison for ST, MT, and TPMS configurations

4.2 Numerical Validation

To ensure the reliability of the proposed multiphysics electromagnetic–thermal coupling model, a validation study was conducted by comparing numerical predictions with experimental measurements in this section. To assess the sensitivity of the numerical predictions to the prescribed coil current, I_{max} was varied by ±5% relative to the baseline values for both coil sizes. The agreement between the numerical and experimental results was quantified using the mean absolute error (MAE) at TCI and TCO. The errors at the two measurement locations were evaluated separately to avoid potential error compensation associated with averaging the temperatures.

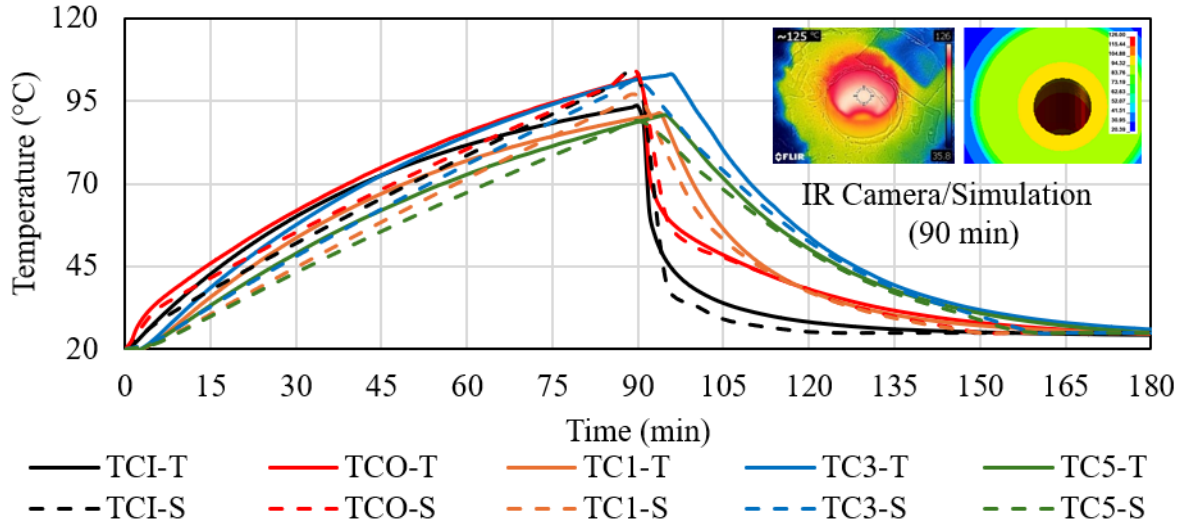
The overall mean absolute error was calculated by combining the prediction errors from both TCI and TCO across all tested CTES configurations. As shown in Table 5, changing I_{max} improved the agreement for some individual configurations but did not consistently improve the predictions across all geometries. For the 200 mm coil, 110 A yielded the lowest overall MAE of 5.71 °C, compared with 6.77 °C and 9.26 °C for 104.5 A and 115.5 A, respectively. Similarly, for the 150 mm coil, the baseline current of 130 A produced the lowest overall MAE of 11.37 °C, compared with 16.83 °C at 123.5 A and 12.77 °C at 136.5 A. Although the ±5% cases provided lower errors for certain individual temperature locations, their performance was less consistent when applied across the ST, MT, and TPMS configurations. Therefore, 110 A and 130 A were selected for the 200 mm and 150 mm coils, respectively, as they provided the most robust overall agreement across the tested CTES configurations.

Table 5 MAE between numerical and experimental temperatures for the current sensitivity analysis.

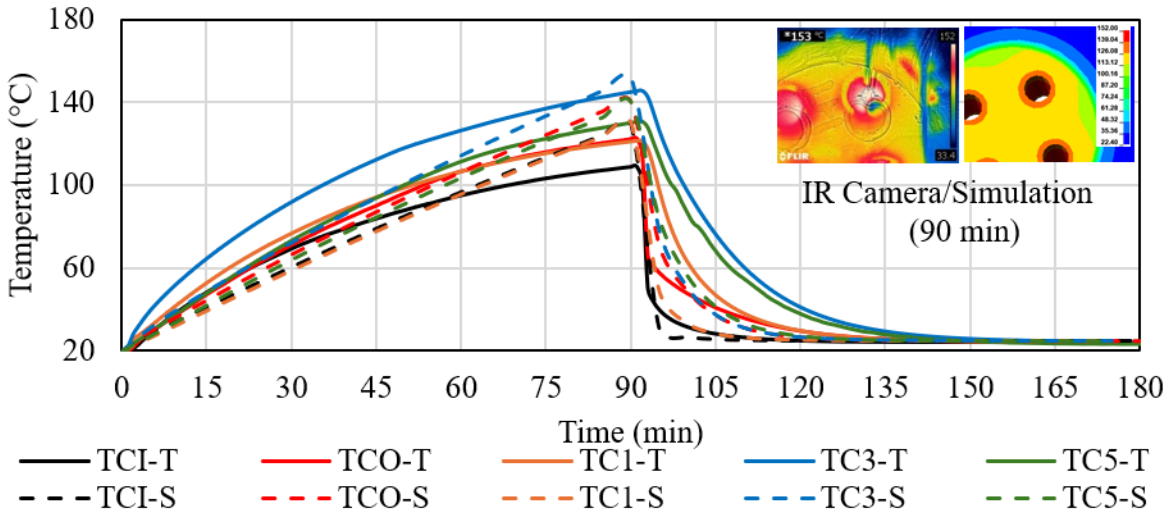
Coil (mm)	Current (A)	TCI MAE (°C)			TCO MAE (°C)			Overall MAE (°C)
		ST	MT	TPMS	ST	MT	TPMS	
200	104.5 (−5%)	6.98	7.31	6.54	8.92	6.43	4.46	6.77
	110	5.07	7.38	7.38	4.28	5.08	5.08	5.71
	115.5 (+5%)	5.66	10.03	12.34	3.12	8.63	15.76	9.26
150	123.5 (−5%)	10.92	5.59	6.85	12.92	8.85	55.87	16.83
	130	9.10	5.96	5.57	6.24	8.94	32.42	11.37
	136.5 (+5%)	7.43	7.60	14.39	1.94	15.59	29.68	12.77

* The overall MAE was calculated from all individual temperature comparison points rather than by averaging the MAE values of the individual configurations.

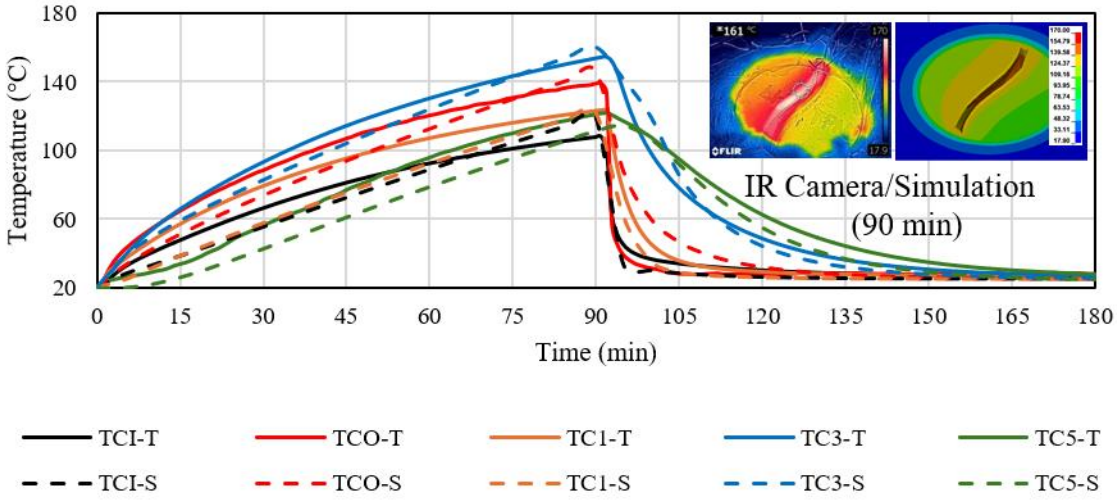
Figure 12 presents the comparison between the experimental and numerical results for the thermal responses of all tested configurations. Overall, the numerical model reproduces the measured temperature evolution and the principal charging–discharging trends with reasonable agreement. In addition to the thermocouple-based comparison, the simulated temperature distributions show good qualitative agreement with the infrared thermal images. The numerical model reproduces the principal spatial characteristics observed experimentally, including the location and overall extent of the high-temperature regions. The predicted temperature fields also capture the radial temperature gradients from the internally heated metallic structure toward the outer concrete region. Although some local differences in temperature magnitude are present, the close correspondence in the overall thermal patterns indicates that the model is capable of representing not only the temporal temperature evolution at discrete measurement locations but also the spatial heat distribution within the CTES specimens.



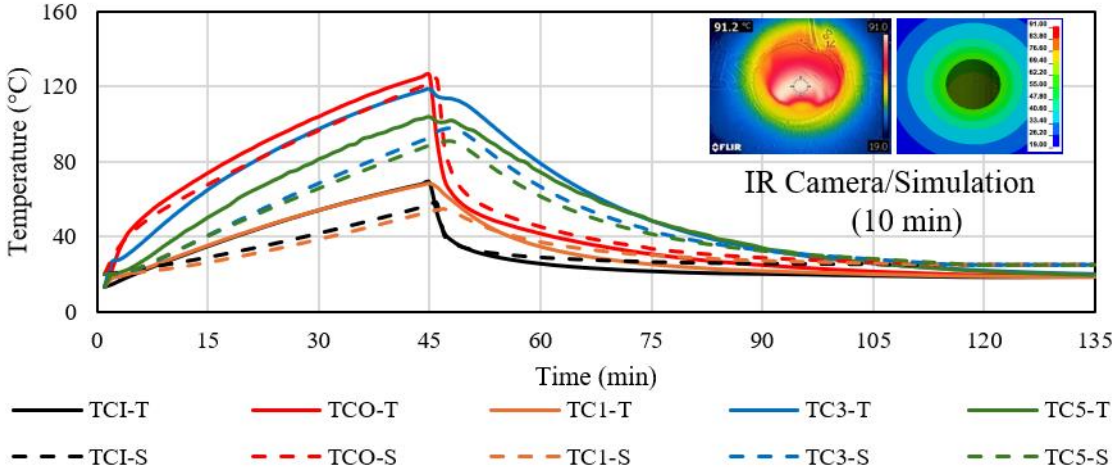
a) ST-200



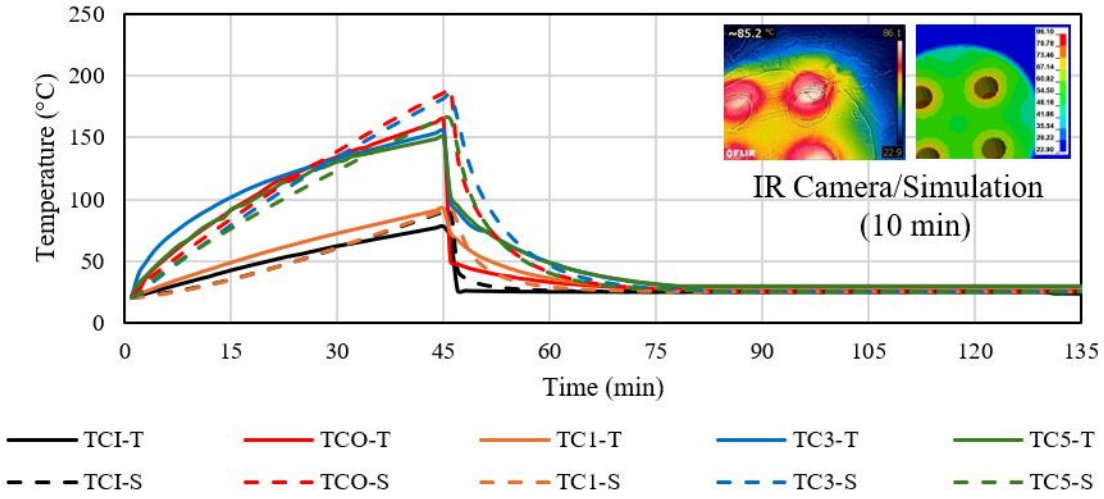
b) MT-200



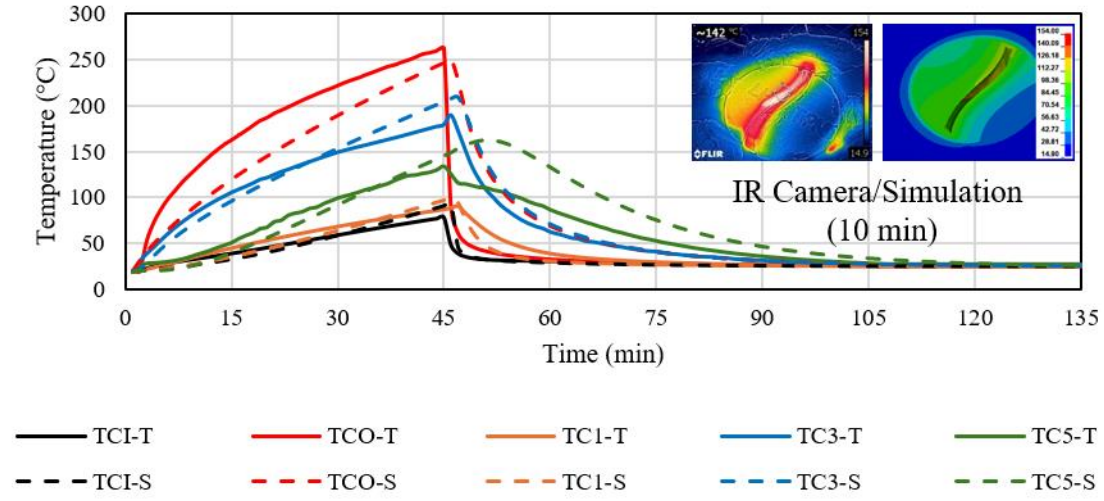
c) TPMS-200



d) ST-150



e) MT-150



f) TPMS-150

Figure 12 Comparison of temperature responses obtained from the experiments (solid line, -T prefix) and the numerical simulations (dashed line, -S prefix). Note different scales used

Table 6 quantitatively evaluates the agreement between the experimental and numerical results using the MAE calculated across TCI, TCO, TC1, TC3, and TC5 at different times during the charging and discharging phases. Overall, the numerical model reproduced the measured temperature evolution with reasonable accuracy across the six configurations. For most of the selected time points, the MAE remained below 10 °C, and the discrepancy generally decreased as the thermal response approached a quasi-steady condition. Larger deviations occurred at several transient stages, with the maximum MAE of 20.36 °C for TPMS-150 at 60 min. This discrepancy was primarily associated with local differences in the predicted cooling response at TCO and TC5 rather than a systematic deviation across all measurement locations. Similar transient discrepancies were observed for MT-200 at 90 min and for several configurations during the earlier heating stage. These deviations may arise from the idealised thermal boundary conditions and geometric representation adopted in the numerical model, together

with the highly localised electromagnetic heating and subsequent heat transfer within the metallic structures. Nevertheless, the generally low MAEs at later stages, together with the agreement in the overall temperature evolution, indicate that the model adequately captures the principal thermal behaviour of the proposed induction-heated CTES system.

Table 6 MAE between experimental and numerical temperatures (°C)

Configuration	ST-200	MT-200	TPMS-200	ST-150	MT-150	TPMS-150
30 min	7.6	11.7	14.3	16.1	5.2	10.2
60 min	5.4	6.3	10.0	6.9	5.3	20.4
90 min	3.6	12.8	7.2	3.4	2.7	3.7
120 min	1.2	6.3	4.8	4.9	2.7	0.6

4.3 Parametric Modelling

The previous sections experimentally and numerically investigated the thermal performance of CTES systems with three different HTF structures under induction heating and forced-air discharge conditions. Using the validated numerical model, this section presents the parametric modelling of the proposed CTES module with a single tube (ST) HTF structure and extends it with the incorporation of a straight fin (ST-S) and a helical fin (ST-H). It should be noted the choice of ST-S and ST-H configurations for the parametric study is justified by the simplicity and prevalence of the single tube and straight/helical fin in the literature [42]. Future research could be conducted for the parametric study of multiple tubes and TPMS HTF structures. Figure 13 presents the geometry of ST-S and ST-H configurations. To be specific, for each fin type, three different fin surface areas (A_s = 0.043, 0.026 and 0.017 m^2) were considered to evaluate the effect of reducing fin material and contact area on the charging and discharging behaviour of the proposed CTES module. The straight-fin configurations consist of four longitudinal fins attached symmetrically around the central tube, while the helical-fin configurations employ a continuous spiral fin with varying extension to achieve equivalent surface areas. This comparison enables a systematic assessment of the trade-offs between heat transfer enhancement, geometric complexity, and material usage for different fin topologies.

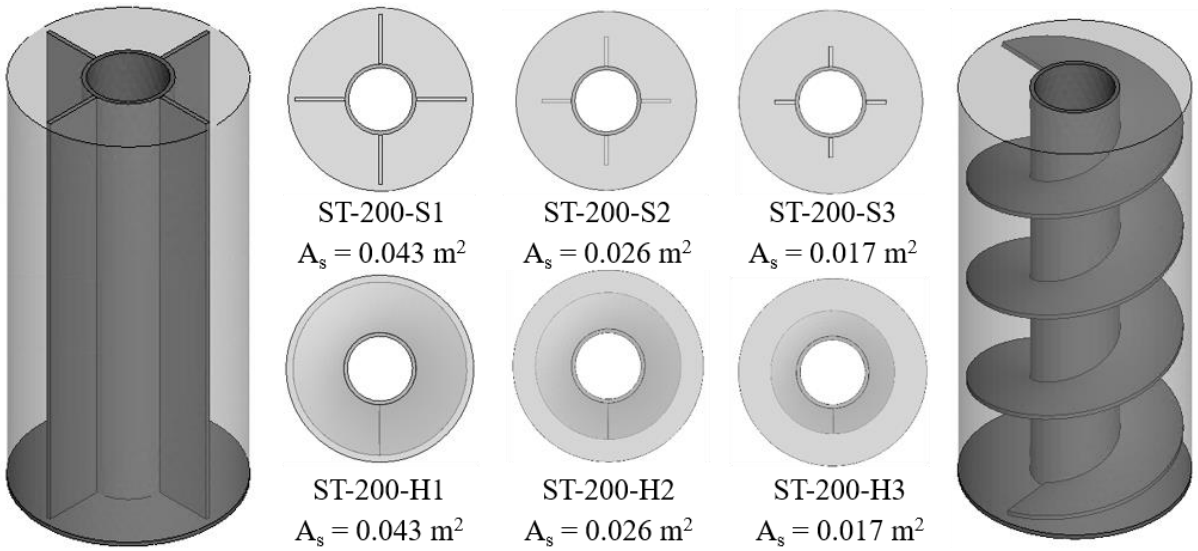


Figure 13 Geometry and surface area comparison of the straight-fin (ST-S) and helical-fin (ST-H) configurations considered in the parametric study.

Figure 14 presents the transient temperature distributions for different CTES configurations investigated in this section. The fin-enhanced configurations further demonstrate that introducing additional metallic conductive structures to the HTF structures can substantially improve induction heating performance. As shown in Figure 14, both straight-fin and helical-fin structures significantly increase heat penetration depth and accelerate temperature propagation within the concrete specimen. As the internal heat transfer area increases from 0.017 to 0.043 m^2, progressively larger high-temperature regions are observed during charging, indicating enhanced conductive heat spreading from the metallic structures into the surrounding concrete.

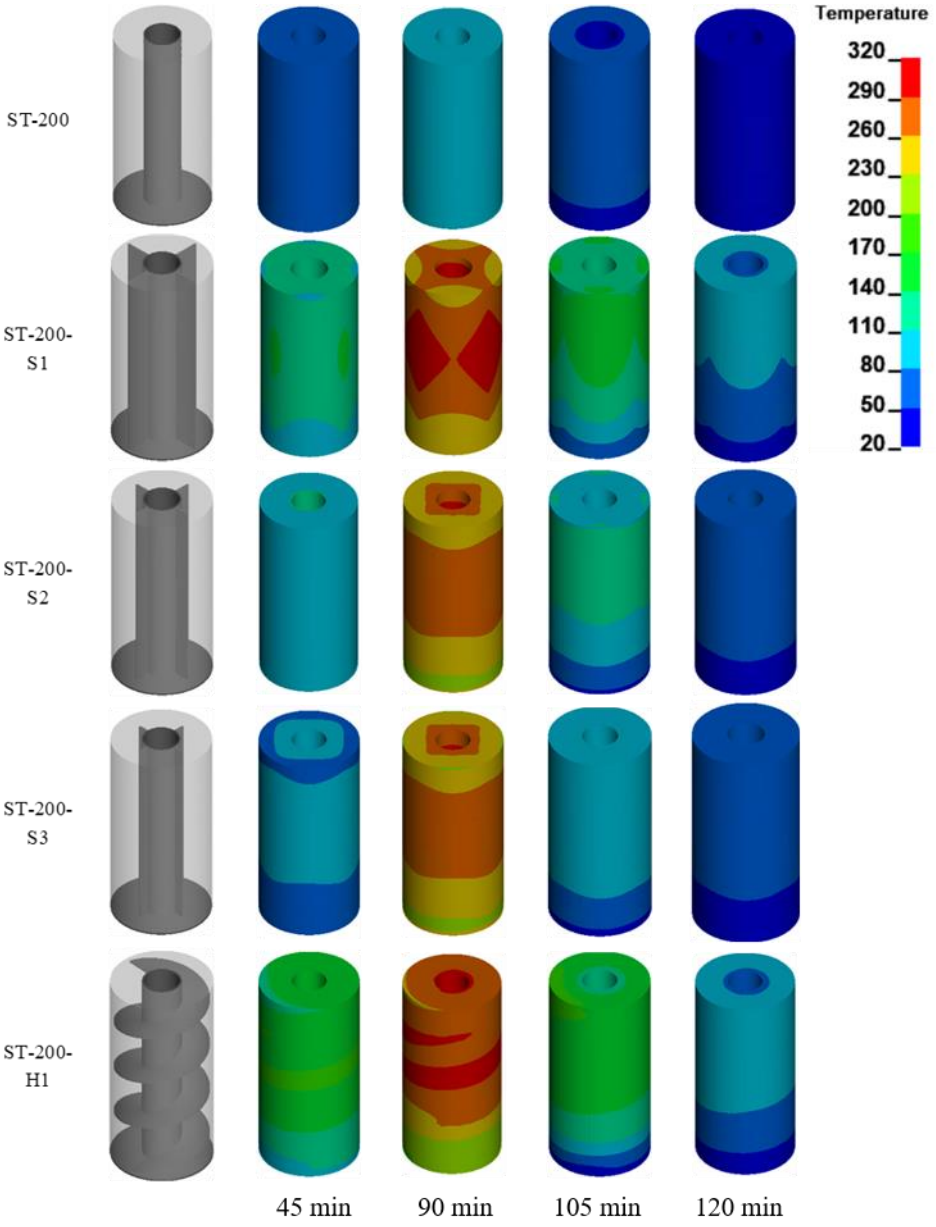
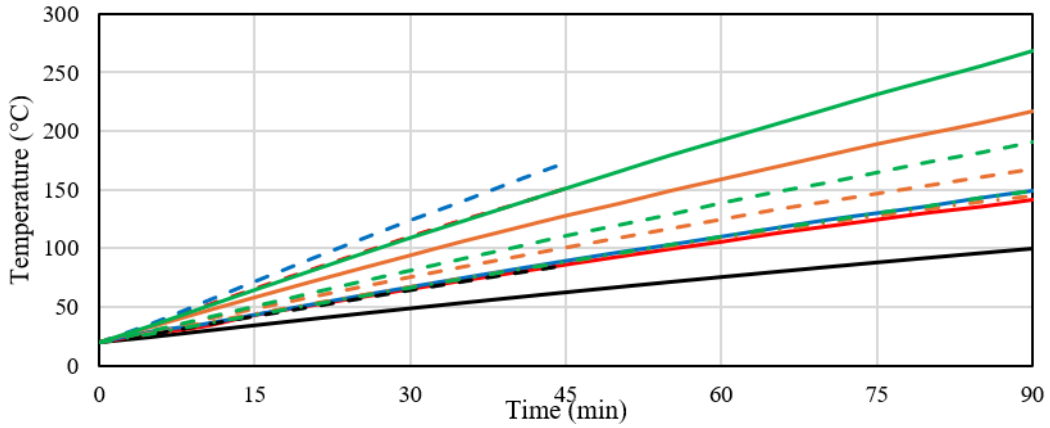


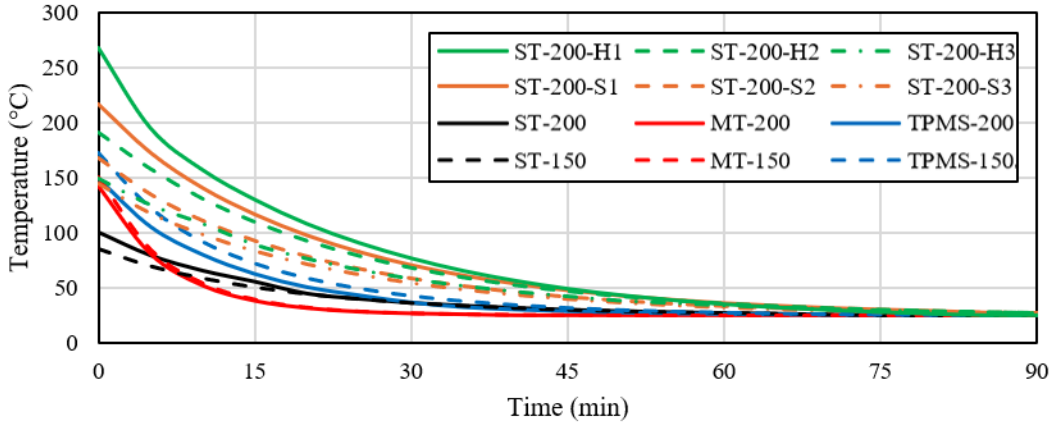
Figure 14 Transient temperature distributions numerical results for various CTES configurations during charging and discharging

Figure 15 presents the average concrete temperature evolution of various CTES modules during induction thermal charging and forced-air discharging conditions. The results clearly demonstrate that both fin topology and effective heat transfer area strongly influence the induction heating efficiency and subsequent thermal discharge behaviour of the system. In general, increasing A_s significantly enhances the thermal interaction between the inductively heated metallic part and the surrounding concrete, resulting in faster temperature rise, higher average concrete temperatures, and improved discharging capability. For the straight-fin configurations (ST-200-S1 to ST-200-S3), the charging and discharging performance decreases progressively as the heat-transfer surface area is reduced. During induction charging, the larger fin area promotes more effective conductive heat spreading from the metallic airway into the concrete domain, thereby reducing localised overheating near the induction-heated

core and improving radial thermal diffusion. Consequently, ST-200-S1 achieves the highest average charging power among the straight-fin cases. In contrast, ST-200-S3 exhibits slower temperature propagation and reduced thermal uniformity due to the smaller conductive interface between the metallic structure and concrete. A similar trend is observed for the helical-fin configurations (ST-200-H1 to ST-200-H3). Increasing the helical fin surface area substantially improves both induction charging and thermal discharge performance. Among all investigated cases, ST-200-H1 demonstrates the highest charging and discharging efficiency. Compared with straight fins possessing similar surface areas, the helical fins exhibit more uniform temperature distributions and enhanced thermal penetration throughout the concrete volume, as presented in Figure 14.



(a) $T_{c,avg}$ during charging

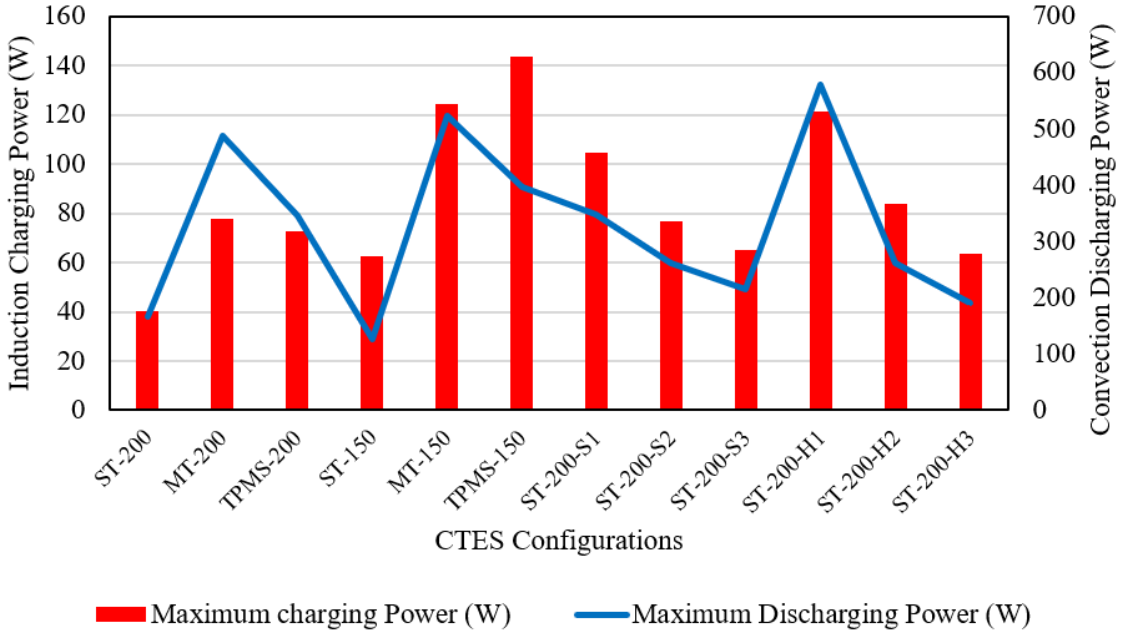


(b) $T_{c,avg}$ during discharging

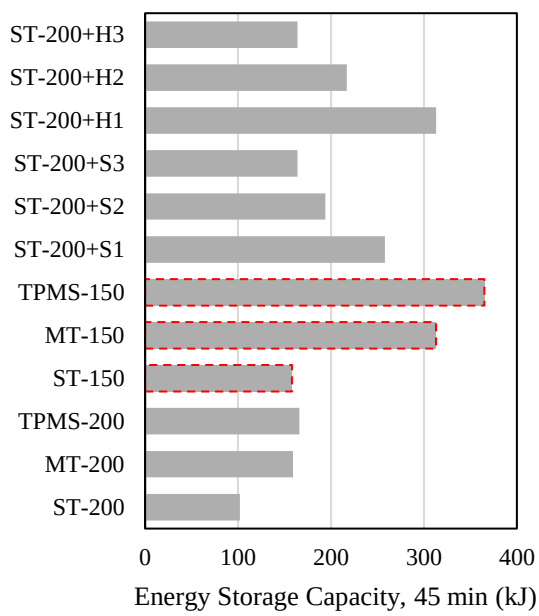
Figure 15 Average concrete temperature $T_{c,avg}$ evolution during induction charging and forced convective discharging for different CTES HTF configurations

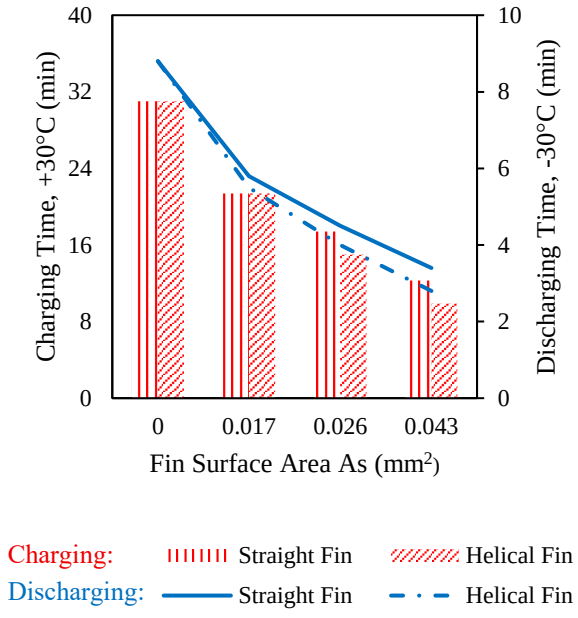
The charging/discharging power and energy storage capacity after 45 min of charging is compared in Figure 16(a). Figure 16(c) further compares the charging and discharging times (to increase/decrease the average concrete temperature by 30 ºC) associated with different fin surface areas. Both the straight-fin and helical-fin configurations showed clear improvement over the conventional ST system. Increasing fin surface area consistently enhanced the stored

thermal energy, indicating that enlarged metallic–concrete contact area promoted more efficient volumetric heat distribution during induction charging. Like the observation in Figure 15, the helical-fin configurations generally exhibited superior performance compared with the straight-fin cases at similar surface areas, which can be attributed to their continuous spiral conductive pathways and improved spatial heat distribution characteristics. Increasing fin area significantly reduced the charging time required to achieve a 30 °C average temperature increase. For example, the charging time decreased from approximately 31 min for the conventional ST configuration to below 15 min for the largest fin-enhanced cases. At the same time, larger fin surface areas also accelerated the initial convective heat extraction during discharging, leading to shorter times for a 30 °C temperature reduction. This behaviour reflects the dual role of enhanced metallic structures in simultaneously improving both heat charging and heat extraction processes. In particular, Figure 15 and Figure 16(a) show that for the proposed CTES module, the ST-200-H1 configuration achieves better charging/discharging behaviour compared to the MT-200 and TPMS-200 configurations, despite employing a geometrically simpler HTF structure. This behaviour is attributed to the continuous spiral conductive pathways provided by the helical geometry, which promote more distributed heat transfer and enhanced interaction between the metallic structure and the surrounding concrete. From a (scaled-up) manufacturing perspective, the ST-200-H1 configuration is also more feasible due to its relatively simple geometry and potentially low fabrication cost. A further comparison between the 150 and 200 mm coil cases provides useful insight into the trade-off between electromagnetic coupling and practical system design. Reducing the coil diameter generally strengthens the electromagnetic interaction with the metallic structure and therefore improves the heating response. However, a larger coil may offer practical advantages for scaled up CTES systems, including greater geometric flexibility, easier accommodation of larger storage modules, and increased clearance for insulation, structural components, and maintenance. The present results show that several fin-enhanced configurations tested with the 200 mm coil achieved thermal responses comparable to those obtained with the smaller 150 mm coil. This suggests that optimisation of the internal metallic heat-transfer structure can partially compensate for the weaker coupling associated with a larger coil, while retaining the practical benefits of a more spacious coil arrangement.



(a) P_{charge} and $P_{discharge}$ Comparison





(b) Energy Storage Capacity at 45 min (c) Charging/Discharging Time (ST-200)

Figure 16 Influence of fin geometry and internal heat transfer area on the charging and discharging behaviour of CTES configurations

5. Conclusions and Outlook

Main lessons learned from this experimental and numerical study and future work arising from it are summarised next.

5.1 Conclusions

This study investigated the thermal performance of inductively heated CTES systems incorporating different HTF heat exchanger structures. A unified framework integrating induction charging, forced convective discharging, experimental validation, and multiphysics modelling was developed to systematically evaluate the influence of induction heating and HTF structures on the performance of the proposed CTES module. Based on the experimental and numerical results, conclusions are drawn as follows:

1. The experimental results demonstrated that different HTF configurations significantly enhanced the inductive charging behaviour of the proposed CTES. Among all investigated cases, the TPMS-150 configuration achieved the highest charging performance, reaching an average concrete temperature of approximately 173 °C within 45 min and reducing the charging time required for a 30 °C temperature increase by approximately 73% compared with the ST-200 configuration. The enhanced performance was primarily attributed to improved electromagnetic coupling, increased heat-transfer surface area, and improved conductive heat-transfer pathways.

2. The coupled multiphysics model successfully captured the electromagnetic induction process, transient heat transfer behaviour, and forced-air convective cooling characteristics of the proposed CTES system. A ±5% coil-current sensitivity analysis across the ST, MT, and TPMS configurations identified 110 A and 130 A as the most representative currents for the 200 mm and 150 mm coils, respectively, yielding the lowest overall MAEs of 5.7 °C and 11.4 °C. The consistent agreement across different airway geometries and temperature measurement locations confirms the model's capability to reproduce the principal thermal response of the inductively heated CTES system and supports its application in the subsequent parametric study.

3. The parametric study demonstrated that fin-assisted HTF structures (ST-200-S1 and ST-200-H1) can substantially improve the thermal charging and discharging performance of the proposed inductive heating CTES system while maintaining relatively simple geometric configurations. Increasing the internal metallic surface area enhanced average charging power, energy storage capacity, and thermal diffusion within the concrete medium.

4. Among the investigated fin-enhanced cases, the helical-fin structures generally exhibited superior thermal performance compared with other investigated configurations. In particular, the ST-200-H1 configuration achieved an average charging temperature of approximately 151 °C after 45 min, corresponding to a stored thermal energy of approximately 313 kJ and an average charging power exceeding 100 W. The charging time required for a 30 °C average temperature increase was reduced from approximately 31 min for the conventional ST-200 configuration to below 10 min for the ST-200-H1 case, representing a reduction of approximately 68%.

5.2 Outlook

Future work should focus on extending the present laboratory-scale investigation towards larger and more application-relevant CTES systems. Particular attention should be given to

optimising the metallic heat-transfer network and induction-coil arrangement to balance charging rate, discharge performance, pressure drop, energy-storage capacity, and electromagnetic efficiency. Further experimental studies under repeated charging–discharging cycles are also required to assess long-term thermal stability, material durability, and possible degradation of the concrete–metal interfaces. In addition, system-level optimisation incorporating power-electronics efficiency, thermal losses, and scale-up effects would help establish the practical energy and economic performance of induction-assisted CTES. The validated multiphysics framework developed in this study provides a useful basis for these future investigations and for designing integrated thermal storage systems with controllable and rapid charging capability. Future studies should also focus on topology optimisation of the internal HTF and fin structures to further improve the thermo-hydraulic performance of the proposed induction-heated CTES systems, particularly the coupled interactions among EM heating behaviour, conductive heat spreading, and airflow dynamics.

Acknowledgement

This research is supported by the Australian Research Council Discovery Early Career Researcher Award (ARC DE240100548) and the Program of China Scholarship Council (CSC NO. 202106090007). Support from The University of Melbourne's Research Computing Services in the computational analysis is much appreciated.

Reference

[1] W. Lu *et al.*, "A novel solids-based electro-thermal energy storage system utilizing electromagnetic induction: Conceptual design and theoretical analysis," *Energy Conversion and Management,* vol. 340, p. 119974, 2025/09/15/ 2025, doi: https://doi.org/10.1016/j.enconman.2025.119974.

[2] G. Hou, Y. Fan, and J. Wang, "Intelligent fuzzy neural network modeling for flexible operation of combined heat and power plant with heat-power decoupling technology," *Energy,* vol. 309, p. 133099, 2024.

[3] Z. Su *et al.*, "Opportunities and strategies for multigrade waste heat utilization in various industries: A recent review," *Energy Conversion and Management,* vol. 229, p. 113769, 2021.

[4] G. Alva, Y. Lin, and G. Fang, "An overview of thermal energy storage systems," *Energy,* vol. 144, pp. 341-378, 2018/02/01/ 2018, doi: https://doi.org/10.1016/j.energy.2017.12.037.

[5] H. Mahon, D. O'Connor, D. Friedrich, and B. Hughes, "A review of thermal energy storage technologies for seasonal loops," *Energy,* vol. 239, p. 122207, 2022/01/15/ 2022, doi: https://doi.org/10.1016/j.energy.2021.122207.

[6] B. R. Knudsen, D. Rohde, and H. Kauko, "Thermal energy storage sizing for industrial waste-heat utilization in district heating: A model predictive control approach," *Energy,* vol. 234, p. 121200, 2021/11/01/ 2021, doi: https://doi.org/10.1016/j.energy.2021.121200.

[7] Q. Huang *et al.*, "Electrified thermal energy storage," *Nature Reviews Clean Technology,* pp. 1-18, 2026.

[8] M. N. I. Maruf, G. Morales-Espana, J. Sijm, N. Helistö, and J. Kiviluoma, "Classification, potential role, and modeling of power-to-heat and thermal energy storage in energy systems: A review," *Sustainable Energy Technologies and Assessments,* vol. 53, p. 102553, 2022.

[9] C. C. Kwasi-Effaha and O. Okpako, "Comprehensive review of emerging trends in thermal energy storage mechanisms, materials and applications," *Frontiers in Energy Research,* vol. 13, p. 1651471, 2025.

[10] K. Vigneshwaran, G. S. Sodhi, A. Guha, P. Muthukumar, and S. Subbiah, "Coupling strategy of multi-module high temperature solid sensible heat storage system for large scale application," *Applied Energy,* vol. 278, p. 115665, 2020/11/15/ 2020, doi: https://doi.org/10.1016/j.apenergy.2020.115665.

[11] M. E. H. Attia *et al.*, "Performance enhancement of hemispherical solar stills using different shapes of basin liners (sinusoidal and half-circle) incorporated with inverted solar collectors," *Environment, Development & Sustainability,* vol. 26, no. 7, 2024.

[12] N. Georgousis, J. Diriken, M. Speetjens, and C. Rindt, "Comprehensive review on packed-bed sensible heat storage systems," *Journal of Energy Storage,* vol. 121, p. 116516, 2025/06/15/ 2025, doi: https://doi.org/10.1016/j.est.2025.116516.

[13] S. Barbhuiya, B. B. Das, and M. Idrees, "Thermal energy storage in concrete: A comprehensive review on fundamentals, technology and sustainability," *Journal of Building Engineering,* vol. 82, p. 108302, 2024.

[14] C. Prieto, E. Borri, M. C. Pavon-Moreno, G. Zsembinszki, and L. F. Cabeza, "A technical and economic comparison between concrete and latent thermal energy storage for concentrated solar power applications," *Applied Thermal Engineering,* vol. 275, p. 126823, 2025/09/15/ 2025, doi: https://doi.org/10.1016/j.applthermaleng.2025.126823.

[15] X. Liang and C. Wu, "Investigation on thermal conductivity of steel fiber reinforced concrete using mesoscale modeling," *International Journal of Thermophysics,* vol. 39, no. 12, p. 142, 2018.

[16] M. Rahjoo, E. Rojas, G. Goracci, J. J. Gaitero, P. Martauz, and J. S. Dolado, "A numerical study of geopolymer concrete thermal energy storage: Benchmarking TES module design and optimizing thermal performance," *Journal of Energy Storage,* vol. 74, p. 109389, 2023/12/25/ 2023, doi: https://doi.org/10.1016/j.est.2023.109389.

[17] B. Król, "Analysis of the use of energy storage in the form of concrete slabs as a method for sustainable energy management in a system with active thermal insulation and solar collectors," *Sustainability,* vol. 16, no. 17, p. 7645, 2024.

[18] K. Vigneshwaran, G. Singh Sodhi, P. Muthukumar, and S. Subbiah, "Concrete based high temperature thermal energy storage system: Experimental and numerical studies," *Energy Conversion and Management,* vol. 198, p. 111905, 2019/10/15/ 2019, doi: https://doi.org/10.1016/j.enconman.2019.111905.

[19] M. G. Gado, O. Al-Ketan, M. Aziz, R. A. Al-Rub, and S. Ookawara, "Triply Periodic Minimal Surface Structures: Design, Fabrication, 3D Printing Techniques, State-of-the-Art Studies, and Prospective Thermal Applications for Efficient Energy Utilization," *Energy Technology,* vol. 12, no. 5, p. 2301287, 2024.

[20] L. Prasad and P. Muthukumar, "Design and optimization of lab-scale sensible heat storage prototype for solar thermal power plant application," *Solar Energy,* vol. 97, pp. 217-229, 2013/11/01/ 2013, doi: https://doi.org/10.1016/j.solener.2013.08.022.

[21] J. Wang, K. Chen, M. Zeng, T. Ma, Q. Wang, and Z. Cheng, "Assessment of flow and heat transfer of triply periodic minimal surface based heat exchangers," *Energy,* vol. 282, p. 128806, 2023/11/01/ 2023, doi: https://doi.org/10.1016/j.energy.2023.128806.

[22] H. Xu, W. Yu, Y. Zhang, S. Ma, Z. Wu, and X. Liu, "Flow and heat transfer performance of bionic heat transfer structures with hybrid triply periodic minimal surfaces," *Applied Energy,* vol. 351, p. 121847, 2023/12/01/ 2023, doi: https://doi.org/10.1016/j.apenergy.2023.121847.

[23] K. Yan, H. Deng, Y. Wu, J. Wang, and Y. Huang, "Effects of lattice geometric manipulation on thermo-hydraulic performance of Gyroid-structured heat exchanger: A numerical study," *International Journal of Heat and Mass Transfer,* vol. 248, p. 127217, 2025.

[24] X. Zhang *et al.*, "Enhanced melting behavior of phase change materials using anisotropic Primitive sheet-networks triply periodic minimal surface structure," *Energy,* vol. 328, p. 136624, 2025/08/01/ 2025, doi: https://doi.org/10.1016/j.energy.2025.136624.

[25] X. Zhang *et al.*, "Topology optimization for accelerating thermal charging in TPMS-based latent heat storage units: A rapid method for determining porosity distribution," *Energy,* vol. 351, p. 140881, 2026/05/15/ 2026, doi: https://doi.org/10.1016/j.energy.2026.140881.

[26] T. Zhang, X. Deng, M. Zhao, H. Zhou, and D. Z. Zhang, "Experimental study on the thermal storage performance of phase change materials embedded with additively manufactured triply periodic minimal surface architected lattices," *International Journal of Heat and Mass Transfer,* vol. 199, p. 123452, 2022.

[27] J. Wang *et al.*, "Experimental and numerical analysis of functionally graded hybrid TPMS heat exchangers for enhanced flow and thermal performance," *Applied Thermal Engineering,* vol. 264, p. 125528, 2025.

[28] M. Wu, M. Li, C. Xu, Y. He, and W. Tao, "The impact of concrete structure on the thermal performance of the dual-media thermocline thermal storage tank using concrete as the solid medium," *Applied Energy,* vol. 113, pp. 1363-1371, 2014/01/01/ 2014, doi: https://doi.org/10.1016/j.apenergy.2013.08.044.

[29] N. Hoivik *et al.*, "Long-term performance results of concrete-based modular thermal energy storage system," *Journal of Energy Storage,* vol. 24, p. 100735, 2019/08/01/ 2019, doi: https://doi.org/10.1016/j.est.2019.04.009.

[30] P. Cui, W. Zhu, H. Ji, H. Chen, C. Hang, and M. Li, "Analysis and optimization of induction heating processes by focusing the inner magnetism of the coil," *Applied Energy,* vol. 321, p. 119316, 2022/09/01/ 2022, doi: https://doi.org/10.1016/j.apenergy.2022.119316.

[31] Q. Huang *et al.*, "Electrified thermal energy storage," *Nature Reviews Clean Technology,* vol. 2, no. 2, pp. 89-106, 2026.

[32] W. Li *et al.*, "Graphene-based phase-change composites for thermal energy storage, conversion, and applications," *Journal of Energy Storage,* vol. 122, p. 116619, 2025.

[33] R. Liberatore, D. Nicolini, M. Lanchi, and A. Miliozzi, "Experimental Testing of New Concrete-Based, Medium-Temperature Thermal Energy Storage Charged by Both a Thermal and Electrical Power Source," *Energies,* vol. 18, no. 13, p. 3511, 2025.

[34] C. Liu, J. Han, R. Lu, and J. Liu, "Explorative study on an online induction heating-based pilger rolling process for seamless treatment of high-frequency welded pipes," *Materials Today Communications,* vol. 35, p. 106068, 2023.

[35] R. T. Ibekwe, "Induction heating of firebricks for the large-scale storage of nuclear and renewable energy," Massachusetts Institute of Technology, 2018.

[36] Q. Liu, Y. Yu, W. Li, Y. Ao, B. Su, and J. Zhou, "Multi-physical coupling field investigation on phase transition of molten salt heated by electromagnetic induction for thermal energy storage applications," *Applied Thermal Engineering,* vol. 280, p. 128234, 2025/12/01/ 2025, doi: https://doi.org/10.1016/j.applthermaleng.2025.128234.

[37] X. ZHANG, Z. XING, Q. FU, C. ZHANG, and L. JIANG, "Multiphysics study of induction heating for solid electric heat storage devices," *Energy Storage Science and Technology,* vol. 12, no. 12, p. 3761, 2023.

[38] A. Group. "AIS STONEWOOL Blanket Technical Data Sheet." AIS Group. https://www.ais-group.com.au/wp-content/uploads/2025/07/AIS_AIS-Stonewool-Blanket_TDS_0725-1-V2.pdf (accessed.

[39] M. Metal. "Maraging Steel 300 Material Data Sheet." Modulus Metal. https://www.modulusmetal.com/maraging-steel-300-material-data-sheet/ (accessed.

[40] A. Gil *et al.*, "State of the art on high temperature thermal energy storage for power generation. Part 1—Concepts, materials and modellization," *Renewable and Sustainable Energy Reviews,* vol. 14, no. 1, pp. 31-55, 2010/01/01/ 2010, doi: https://doi.org/10.1016/j.rser.2009.07.035.

[41] C. Xu, Z. Wang, Y. He, X. Li, and F. Bai, "Sensitivity analysis of the numerical study on the thermal performance of a packed-bed molten salt thermocline thermal storage system," *Applied Energy,* vol. 92, pp. 65-75, 2012/04/01/ 2012, doi: https://doi.org/10.1016/j.apenergy.2011.11.002.

[42] L. Tu and T. Nguyen, "A comparative study of different fin designs for enhancing the performance of concrete thermal energy storage," *Energy,* vol. 349, p. 140677, 2026/04/15/ 2026, doi: https://doi.org/10.1016/j.energy.2026.140677.

[43] C. Yuan, X. Gao, H. K. Wong, B. Feng, and J. Xu, "A multiphysics computational framework for cylindrical battery behavior upon mechanical loading based on LS-DYNA," *Journal of the Electrochemical Society,* vol. 166, no. 6, p. A1160, 2019.

[44] T. D. Economon, "Simulation and adjoint-based design for variable density incompressible flows with heat transfer," *AIAA Journal,* vol. 58, no. 2, pp. 757-769, 2020.

[45] I. R. Cal, J. L. Cercos-Pita, and D. Duque, "The incompressibility assumption in computational simulations of nasal airflow," *Computer Methods in Biomechanics and Biomedical Engineering,* vol. 20, no. 8, pp. 853-868, 2017.

[46] D. J. Griffiths, *Introduction to electrodynamics*. Cambridge University Press, 2023.

[47] P. L'Eplattenier, G. Cook, C. Ashcraft, M. Burger, J. Imbert, and M. Worswick, "Introduction of an electromagnetism module in LS-DYNA for coupled mechanical-thermal-electromagnetic simulations," *Steel research international,* vol. 80, no. 5, pp. 351-358, 2009.

[48] M. Duhovic, P. Mitschang, M. Maier, I. Caldichoury, and P. L'Eplattenier, "Advance in simulating the processing of composite materials by electromagnetic induction," in *9th European LS-Dyna Conference*, 2013.

[49] I. Caldichoury, R. R. Paz, and F. Del Pin, "ICFD Theory Manual: Incompressible Fluid Solver in LS-DYNA," Livermore Software Technology Corporation (LSTC), Livermore, CA, 2014. [Online]. Available: https://ftp.lstc.com/anonymous/outgoing/inaki/docs/pdf_icfd/ICFD_theory.pdf

[50] C. C. Kwasi-Effah, O. Ibhadode, and A. Qureshi, "Thermo-hydraulic performance characteristics of novel G-Prime and FRD Triply Periodic Minimal Surface (TPMS) geometries," *International Communications in Heat and Mass Transfer,* vol. 159, p. 108226, 2024/12/01/ 2024, doi: https://doi.org/10.1016/j.icheatmasstransfer.2024.108226.

[51] S. Panchal *et al.*, "Numerical simulation of cooling plate using K-epsilon turbulence model to cool down large-sized graphite/LiFePO4 battery at high C-rates," *World Electric Vehicle Journal,* vol. 13, no. 8, p. 138, 2022.
[52] T. L. Bergman, *Fundamentals of heat and mass transfer*. John Wiley & Sons, 2011.
[53] M. Fisk, M. Ristinmaa, A. Hultkrantz, and L.-E. Lindgren, "Coupled electromagnetic-thermal solution strategy for induction heating of ferromagnetic materials," *Applied Mathematical Modelling,* vol. 111, pp. 818-835, 2022/11/01/ 2022, doi: https://doi.org/10.1016/j.apm.2022.07.009.
[54] U. T. Shami and T. A. Shami, "An adaptive load-matching method for the induction heating coil with DC power supply," *International Journal of Circuit Theory and Applications,* vol. 52, no. 10, pp. 5025-5041, 2024.
[55] B. En, "1-2: 2004 Eurocode 2: Design of concrete structures-Part 1-2: General rules-Structural fire design," *European Standards, London,* 2004.
[56] I. Ansys, *LS-DYNA Keyword User's Manual, Volume III: Multi-Physics Solvers*, Release 16 ed. Ansys, Inc., 2025.
[57] I. Caldichoury, P. L'Eplattenier, and M. Duhovic, "LS-DYNA R7: coupled multiphysics analysis involving electromagnetism (EM), incompressible CFD (ICFD) and solid mechanics thermal solver for conjugate heat transfer problem solving," in *Proceedings of the 9th European LS-DYNA users conference*, 2013.
[58] B. Wang and M. Yan, "Research on the heating effect evaluation of the electromagnetic induction heating system at low temperature based on the electrochemical-thermal coupling model," *Journal of Energy Storage,* vol. 87, p. 111348, 2024/05/15/ 2024, doi: https://doi.org/10.1016/j.est.2024.111348.